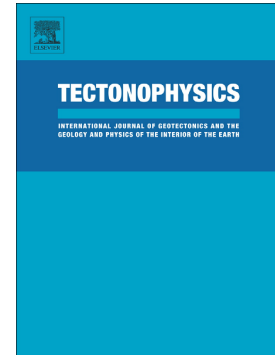


## Accepted Manuscript

Ambient seismic noise tomography of SW Iberia integrating seafloor- and land-based data

Carlos Corela, Graça Silveira, Luis Matias, Martin Schimmel, Wolfram H. Geissler



PII: S0040-1951(17)30058-6  
DOI: doi: [10.1016/j.tecto.2017.02.012](https://doi.org/10.1016/j.tecto.2017.02.012)  
Reference: TECTO 127404

To appear in: *Tectonophysics*

Received date: 29 June 2016  
Revised date: 6 January 2017  
Accepted date: 13 February 2017

Please cite this article as: Carlos Corela, Graça Silveira, Luis Matias, Martin Schimmel, Wolfram H. Geissler , Ambient seismic noise tomography of SW Iberia integrating seafloor- and land-based data. The address for the corresponding author was captured as affiliation for all authors. Please check if appropriate. Tecto(2017), doi: [10.1016/j.tecto.2017.02.012](https://doi.org/10.1016/j.tecto.2017.02.012)

This is a PDF file of an unedited manuscript that has been accepted for publication. As a service to our customers we are providing this early version of the manuscript. The manuscript will undergo copyediting, typesetting, and review of the resulting proof before it is published in its final form. Please note that during the production process errors may be discovered which could affect the content, and all legal disclaimers that apply to the journal pertain.

**Ambient seismic noise tomography of SW Iberia integrating seafloor- and land-based data**

Carlos Corela<sup>1</sup>, Graça Silveira<sup>1, 2</sup>, Luis Matias<sup>1</sup>, Martin Schimmel<sup>3</sup> and Wolfram H. Geissler<sup>4</sup>

(1) Instituto Dom Luiz, Faculdade de Ciências, Universidade de Lisboa, 1749-016 Lisboa, Portugal

(ccorela@fc.ul.pt, mdsilveira@fc.ul.pt, lmmatias@fc.ul.pt)

(2) Instituto Superior de Engenharia de Lisboa (ISEL), Lisboa, Portugal (mdsilveira@fc.ul.pt)

(3) Instituto de Ciencias de la Tierra Jaume Almera", CSIC, C/Lluis Solé I Sabaris s/n, 08028 Barcelona Spain (schimmel@ictja.csic.es)

(4) Alfred-Wegener Institut Bremerhaven, Germany (Wolfram.Geissler@awi.de)

**Abstract**

We used ambient seismic noise recorded by 24 Broadband Ocean Bottom Seismometers (OBS) deployed in the Gulf of Cadiz during the EC funded NEAREST project and seven broadband land stations located in the South of Portugal to image the sedimentary and crustal structure beneath the Eastern Atlantic and SW Iberia. We computed ambient noise cross-correlations to obtain empirical Green's functions (EGFs) between all station pairs using land seismometers and both OBS sensors, seismometers and hydrophones. Despite the great difference in the recording conditions and local crustal structure between the OBSs and land stations, we could compute EGFs, by applying a linear cross-correlation with running absolute mean average time normalization, followed by a time-frequency phase weighted stack. Dispersion analysis was then applied to the EGFs, between 4 and 20s period. The obtained dispersion curves allowed mapping the lateral variation of Rayleigh-wave group velocities, as a function of period. Finally, dispersion curves extracted from each cell of the 2D group velocity maps were inverted, as a function of depth, to obtain the 3D distribution of the shear-wave velocities. The 3-D shear wave velocity model, computed from joint inversion of OBSs and land stations data allowed to estimate the thickness of sediments and crust and the Moho depth. Despite the gap that exists between the OBSs and land station locations, our model displays a good correlation with the known geological structure. The derived sedimentary layer and crustal thicknesses and the obtained Moho depth are locally in agreement with the models proposed by other studies using near vertical, refraction and wide-angle seismic profiling. We conclude that ambient noise tomography could be a valuable tool to

image oceanic domains, and also that it is possible to integrate seafloor- and land-based stations to derive a structure model in the transition domain between continent and ocean.

## Highlights

- Cross-correlation between seismometers and hydrophones
- Time-frequency phase weighted stack as a tool to attenuate incoherent noise
- Joint inversion of data from OBSs and land stations
- 3-D shear wave velocity model of SW Iberia
- Estimation of the sediment and crustal thickness and Moho depth

**Keywords:** seismic noise, surface waves, tomography, ocean bottom seismometers, SW Iberia.

## 1. Introduction

The SW Iberia Margin (SWIM) is located at the eastern end of the Azores-Gibraltar fracture zone, which is part of the Eurasia-Africa plate boundary. The present day tectonic deformation is dominated by compression related to the NW-SE trending convergence of 3.8-5.6 mm/year between the two plates (Nocquet and Calais, 2004; DeMets et al., 2010). This region is deforming across a wide active zone characterized by moderate to strong seismicity that includes a well-documented history of large earthquakes and destructive tsunamis, like the estimated  $M > 8.5$ , 1755 Lisbon earthquake, and represents one of the most important tsunamigenic areas in Europe (Baptista and Miranda, 2009).

The morphology of study area (Fig. 1a), located West of 9°W, is characterized by a complex and irregular topography dominated by large seamounts, deep abyssal plains and massive rises such as the Gorringe Bank, Tagus Abyssal Plain and Horseshoe Abyssal Plain. To the East the topography is smoother and dominated by the Gulf of Cadiz accretionary Wedge (e.g. Gutscher et al., 2002; Gutscher et al., 2009; Terrinha et al., 2009).

The current knowledge of the SWIM tectonics and sedimentary structure is the result of an extensive investigation conducted by numerous European academic institutions during the last 20 years. The data acquired and used to define the structure include multi-channel seismic profiles and multibeam bathymetry (Sartori et al., 1994; Banda et al., 1995; Torelli et al., 1997; Gutscher et

al., 2002; Gràcia et al., 2003a, 2003b, 2010; Zitellini et al., 2004, 2009; Rovere et al., 2004; Terrinha et al., 2009; Gutscher et al., 2009; Martínez-Loriente, et al., 2013). These studies allowed for a comprehensive understanding of the meso-cenozoic and recent tectonics but some uncertainties remain (e.g. Duarte et al., 2013): i) what is the most important source of tectonic stresses in the Gulf of Cadiz, the Eurasia-Nubia plate convergence, or the Gibraltar arc roll-back subduction? ii) Which of the large active faults identified could be responsible for the 1<sup>st</sup> November 1755 Earthquake and tsunami?; iii) the active fault responsible for the M~8.0 28<sup>th</sup> February 1969 remains to be identified.

The knowledge of the deep crustal structure in the SWIM area is much less known since only a few refractions and wide-angle reflections seismic (WAS) profiles have been conducted since the first WAS data acquired, which included sonobuoys, in the Tagus and Horseshoe Abyssal Plains in the mid-1970s (Fig. 1b, Purdy, 1975). On the last decades only two WAS experiments were carried out with OBSs in this area. The SISMAR cruise (2001) which explored the southern part of the Gulf of Cadiz imbricated Wedge (GCIW), the Moroccan Margin and Northern Seine Abyssal plain (Fig. 1b, Gutscher et al., 2002; Construcci et al., 2004; Jaffal et al., 2009) and the NEAREST-SEIS cruise performed at the Gulf of Cadiz and the southern Tagus and northern Horseshoe Abyssal plains (Sallarès et al., 2011, 2013; Martín-Loriente et al., 2014). These sparse studies concentrated on the deep offshore and an integrated image of the subsurface structure in the SW Iberia Margin still needs to be done, particularly in the transitional domain between the deep offshore and the continental onshore.

After the success of the ambient noise tomography during the last decade, there is a growing interest, not only in applying the same analysis to the seismic ambient noise recorded in OBSs, but also in integrating both land- and seafloor-based seismic stations. These integrated studies, with OBSs, require long duration records and numerical algorithms able to efficiently retrieve coherent signal from seismic ambient noise. Up till now, the studies carried out in oceanic domains are scarce (Harmon et al., 2007; Zha et al., 2014) and as well as joint land-ocean studies (Bowden et al., 2016).

In the framework of the EU-funded NEAREST project (Integrated observations from NEAR SourceS of Tsunamis: towards an early warning system) a network of 24 broadband OBSs was deployed in 2007, for eleven months, in the Gulf of Cadiz and offshore Cape St. Vincent (Portugal) (c.f. Fig. 1a), offering a unique opportunity to perform ambient noise tomography using seismic noise recorded at OBSs. The OBSs dataset was completed with data from 7 broadband, land-based stations from

Lisbon University (LX) and the Portuguese (PM) seismic network.

The continuous ambient seismic noise data, recorded in the OBS hydrophone and seismometer, as well as on the selected land stations, were processed together to obtain Rayleigh wave empirical Green's functions (EGFs). The constructed waveforms, having a high contribution from hydrophone ambient noise data, enabled to obtain reliable interstation group-velocity dispersion curves and allowed to perform a 2D group velocity tomography in the period band of 4 - 20 seconds. Finally, we inverted the group velocities curves, for each cell of the 2-D tomographic maps, to obtain a 3-D shear wave velocity model in the area, as a function of depth, enabling us to estimate the thickness of sediments and the Moho depth in the SWIM.

## 2. Geological setting of SWIM

The plethora of available multichannel seismic (MCS) lines together with the nearly complete multibeam coverage, have allowed to define the sedimentary structure and recent tectonics in the SWIM (e.g. Zitellini et al., 2009; Terrinha et al., 2009; Martinez-Loriente et al., 2013; Duarte et al., 2013). The active and most probably active tectonic structures identified (Fig. 1b) support the concept of diffuse plate boundary to accommodate the convergence between Nubia and Eurasia (Sartori et al., 1994; Duarte et al., 2013). Deformation is distributed among numerous thrust faults as well as the SWIM lineaments, which are interpreted as vertical faults with a right-lateral movement (ibid.).

East of 10°W, the most conspicuous feature on the seafloor is the surface expression of the Gulf of Cadiz chaotic body (Fig. 1a) already identified (Bonnin et al., 1975). Today this feature is considered as an accretionary wedge (the Gulf of Cadiz Accretionary Wedge - GCAW) due to the subduction roll-back of the Gibraltar block (e.g. Gutscher et al., 2012) that must have moved during the Miocene; but its current activity is questioned (e.g. Platt and Houseman, 2003). Here the sedimentary cover is very thick and probably only MCS lines obtained with large energy air guns can image the basement, in order to decrease the uncertainty of the sediment thickness map in this area (Gutscher et al., 2009).

To gain knowledge on the thickness, nature of the crust and characteristics of the upper mantle other type of deep penetrating data is required, namely WAS profiles with recording stations both on the ocean and on land to constrain the marginal domains where most of the crustal thinning takes place.

Purdy (1975) published the first crustal model in the area based on the interpretation of profile B/BR (Fig. 1b). Using a nearly coincident MCS line, Rovere et al. (2004) made a re-interpretation of that profile confirming that a very thin crustal layer with velocities  $\sim 6.0$  km/s is underlain by an anomalous mantle with velocities  $\sim 7.4$  km/s. The IAM-6 line acquired during the IAM project (Banda et al., 1995) was recorded on land by several land-stations (Fig. 1b). Despite the absence of recordings in the ocean and reverse shots, the data were interpreted to display a presumed oceanic domain with  $\sim 80$  km width and normal oceanic crust thickness (Gonzalez et al., 1996). The same methodology was also applied to lines IAM-GC1 and IAM-GC2 (Fig. 1b, Gonzalez et al., 2001). The seismic signal along these two profiles did not penetrate below the thick sedimentary cover of the accretionary wedge and only provided information on the thinning of the continental crust in the marginal domain.

Gutscher et al. (2002) presented the first model for the structure of the crust based on OBS seismic recordings. Based on several isolated reflections, they suggested that the crust sampled by profile SISMAR-16 (Fig. 1b) had an oceanic nature with 6-8km thickness. From the same mission, the nearly N-S profile SISMAR-13 (Fig. 1b) sampled by MCS and OBS recordings was modelled by Thiebot et al. (2006) and revised by Klingelhoefer et al. (2016). The thick sedimentary cover below the accretionary wedge precluded an accurate definition of the nature of the crust north of  $35^{\circ}\text{N}$ . Using indirect geophysical evidence these authors propose that the GCAW is also underlain by normal oceanic crust.

In the framework of the NEAREST-SEIS project, two long OBS profiles, P1 and P2 (Fig. 1b) were recorded across the Gulf of Cadiz. Profile P2 (Sallares et al., 2011) was also recorded by land-stations, which allowed to obtain a continuous crustal section from thinned continental crust to the oceanic domain. Profile P1 was recorded from the Tagus Abyssal Plain (Fig. 1b) to the Coral Patch Ridge, crossing the Gorringe Bank and the Horseshoe Abyssal plain. The models obtained by Sallares et al. (2013) and Martinez-Loriente (2014) show a number of different crustal sections, from exhumed to normal oceanic crust. Using these models and an interpretation of the MCS seismic lines building on previous efforts (e.g. Rovere et al., 2004), Martinez-Loriente et al. (2014) proposed a new division of the SWIM crustal domains (Fig. 1b).

According to Martinez-Loriente et al. (2014), the Southern Tagus Abyssal Plain, the Gorringe Bank and the NW Horseshoe Abyssal are underlain lower Cretaceous exhumed mantle that developed during the early stages of the opening of the North Atlantic Ocean. The Accretionary Wedge, the Horseshoe Abyssal Plain and the Seine Abyssal plain are underlain by Jurassic oceanic crust

originated at either the Central Atlantic or the Alpine Tethys oceanic spreading systems. This oceanic domain (Fig. 1b) forms a strip of width 100 to 150 km between the Algarve and NW Moroccan margins, underlain by thinned continental crust. These authors also propose the existence of a major lithospheric structure, namely the “Horseshoe Abyssal Plain Thrust”, which separates at depth the Gorringe Bank domain from the Gulf of Cadiz crustal domain.

Onshore, the continental crust belongs to the South Portuguese Zone (SPZ) of the Iberian Massif, according to the paleogeographic division revised by Julivert et al. (1972). The South Portuguese allochthonous Terrain was accreted during the Variscan orogeny. Two other exotic terrains found in the SPZ affect only the more superficial crustal structure, north of the main investigated area in this work (e.g. Ribeiro et al., 1990). Deep Seismic Sounding profiles show that three layers can be identified in the crystalline continental crust, upper, middle and lower crust (ILIHA Group, 1996, Gonzalez et al., 1998).

The 1<sup>st</sup> November 1755  $M > 8.5$  and the 28<sup>th</sup> February 1969  $M \sim 8.0$  events show that the SW Iberia Margin is able to generate destructive earthquakes and tsunamis. To investigate the micro-seismicity that might be associated with the active tectonic features in the area, the NEAREST project deployed a network of 24 OBSs that operated continuously for almost one year. This network allowed, for the first time, to record and locate numerous low to moderate magnitude earthquakes ( $ML = 2.2-4.8$ ) that were, until then, unknown. This analysis revealed that the seismicity in this area is mostly concentrated at depths 40–60 km, with only few events nucleating shallower than 20 km (Geissler et al., 2010). The nucleation of earthquakes at these depths, combined with structural characteristics of the basement in different parts off SW Iberia suggests that they occur within the upper mantle (e.g., Stich et al., 2010).

The Gorringe Bank Fault (Fig. 1b) is a northwestward-directed thrust located at the northern base of this morphologic feature. This thrust uplifted the seafloor from approximately –5000m to –24m; it reached its paroxysmal activity in Miocene times and has accommodated negligible shortening since then (Sartori et al., 1994; Tortella et al., 1997). The other large faults are the Marquês de Pombal fault, the Horseshoe fault and the the Portimão fault (Fig. 1b). All these have been proposed as the tsunamigenic tectonic sources that may have caused the large event of 1755 (Zitellini et al., 2001; Gràcia et al., 2003; Terrinha et al., 2003).

Despite the large progress seen in the knowledge of tectonics and sedimentary structure of the SWIM region, an integrated image for the deep structure is still lacking. The diverse crustal domains recognized, from exhumed and serpentinized upper mantle, to normal oceanic crust and

thinned continental crust, have very different rheological properties that control the maximum rupture of the largest earthquakes. A detailed characterization of these domains is therefore important to assess the seismic and tsunami hazard in the Southwest Iberia Margin.

### 3. Data and methodology

The NEAREST ocean bottom seismometer experiment started at the end of August 2007 with the deployment of 24 LOBSTER (<http://www.awi.de/en/science/geosciences/geophysics/methods-and-tools/ocean-bottom-seismometer/technology.html>) which means Longterm Ocean Bottom Seismometer for Tsunami and Earthquake Research, from the German DEPAS instrument pool, and ended in August 2008 with the recovery of the instruments. These OBSs were equipped with two different sensors: a Guralp CMG-40T-OBS broadband seismometer, with a flat velocity response between 60s and 50 Hz, and a HTI-04-PCA hydrophone, with a flat response between 100s and 50 Hz. A 24-bit data logger from SEND (Signal Elektronik GmbH), the Geolon MCS, was used to collect the data at a sampling rate of 100 Hz.

Inland, seven broadband stations were chosen to complete the OBSs network extending the study area into the onshore. Although equipped with different sensors and digitizers (two land stations with REFTEK 130-01 data logger and STS-2 seismometer of 120s, three Guralp data logger with Guralp 3T seismometer of 120s and two Guralp data logger with Guralp 3ESPc seismometer of 120s) all the stations have a flat velocity response between 120s and 50 Hz and record continuously at a sampling rate of 100Hz.

The OBSs network was designed with a station spacing of about 50 km, similar with the one observed between land stations. A minimum distance of 100 km separates land and ocean arrays, creating a station gap across the continental platform.

To investigate the seismic noise recorded we computed the Normalized Power Spectra (NPS) for the ocean and land stations during the entire NEAREST experiment. All the spectrograms exhibit a similar pattern, showing that the same ambient seismic noise sources were detected across the entire network. Fig. 2 displays, as example, the NPSs calculated for the seismometer and hydrophone of OBS03 and for MESJ (LX network) land station (for location see Fig.1). The ambient seismic noise sources are dominated by microseismic energy (primary and secondary peaks). These microseismic peaks are generated by different mechanisms, which convert ocean wave's energy into subsurface elastic energy, through a process linking ocean waves, seafloor and

shoreline (Longuet-Higgins, 1950; Hasselmann, 1963). The microseisms are strongest between 4-20 s (Fig. 2) and were identified in all seismic stations independently of their location (see Fig. S1 of the electronic supplementary material).

If the seismic noise sources are homogeneously distributed the Noise Correlation Function (NCF) between two seismic stations correspond to the empirical Green's function (EGFs) of the propagation medium (Lobkis and Weaver, 2001; Campillo and Paul, 2003; Shapiro and Campillo, 2004; Snieder, 2004; Sabra et al., 2005). In theory, the NCF can only represent the EGFs between two points when the balanced net flux of energy becomes zero, however for most of the geographical areas under study, the noise sources are strongest along certain azimuths and there are only a finite number of independent sources (Schimmel et al., 2011). To overcome this limitation, imposed by a seasonal distribution of the seismic sources, the noise cross-correlations should be stacked over long time spans. Under these circumstances the NCF of ambient seismic noise contains information about the distribution of the medium's seismic velocities between the two stations so it can potentially be used to infer subsurface velocity structure at different scales (e.g. Shapiro et al., 2005, Silveira et al., 2013, Matos et al., 2015, Haned et al., 2016). For the following analysis, we will consider the seismometer vertical channel from all seismic stations and the hydrophone channel from the OBSs.

To compute the daily cross-correlations we have followed identical data processing for land and OBSs dataset, like the one described by Bensen et al. (2007). Firstly, the continuous data recorded by the 24 broadband ocean bottom seismometers and by the 7 broadband land stations were evaluated to perform a data quality control (visualizing probabilistic power spectral densities and one-day plots). Next, all the data were down-sampled to 1 Hz and split into one-day-length records.

After instrument response removal and conversion of the seismograms to true ground velocity, a de-meaning, de-trending and band-pass filtering [2-50s] was applied to OBSs and land data records. The considered period range includes the primary and secondary microseisms, and it is also adequate for the interstation distances in our network.

After, the ambient seismic noise data analysis followed six main stages: (1) time and spectral normalization; (2) cross-correlation; (3) stack of the individual cross-correlation; (4) group velocity dispersion measurements; (5) quality control and selection of the acceptable dispersion measurements to perform a 2D tomographic inversion and; (6) inversion of the group velocities as a function of depth to image the 3-D velocity structure.

The time domain normalization reduces the contamination of earthquakes, instrumental irregularities and the effect of non-stationary noise sources near the seismic stations. At this step, two different methods were tested, the 1-bit and the Running Average Mean (RAM) normalization, following the methodology described in Bensen et al. (2007). For the RAM normalization the width of the normalization window was 25 s, half of the maximum period of the passband-filter (ibid.). To assure the attenuation of strong narrow-band signals and to balance the frequency band of noise cross-correlations spectral whitening was applied.

All one-day time series were cross-correlated between all pairs of station-sensor (seismometer vertical channel and hydrophone). To stack individual cross-correlations we tried two different algorithms, the time domain linear stack and the time-frequency domain phase weighted stack (tf-PWS). The tf-PWS procedure (Schimmel and Gallart, 2007; Dias et al., 2015), is an extension of the time-domain phase weighted stack (PWS) developed by Schimmel and Paulssen (1997). Each sample of a linear stack is weighted by a coherence measure, which is independent of amplitude. This weight or phase coherence ranges between 0 and 1 as a function of time. It is one if the instantaneous phases of the signal at a given time are coherent, and zero if they are incoherent.

The tf-PWS, expressed as  $p_{tf}(\tau, f)$  is obtained by:

$$p_{tf}(\tau, f) = S_{1s}(\tau, f) c_{tf}(\tau, f) = S_{1s}(\tau, f) \left| \frac{1}{N} \sum_{j=1}^N \frac{S_j(\tau, f) e^{i\pi f \tau}}{|S_j(\tau, f)|_j} \right|^v$$

where  $S_j(\tau, f)$  is the S-transform (Stockwell et al., 1996; Schimmel and Gallart, 2005; Schimmel et al., 2011) of the  $j^{\text{th}}$  time-series and  $S_{1s}(\tau, f)$  is the S-transform of the linear stacking of all  $N$  time-series (cross-correlograms). The phase coherence  $c_{tf}(\tau, f)$  is used to down-weight the incoherent portions of the linear stacking in the time-frequency domain (Schimmel et al., 2011) and  $v$  is a variable for tuning the transition between coherent and less coherent signal summation.

A combination of the described processing steps, with two time domain normalization approaches and two stacking methods were tested with a subset of the entire data. An example of these four different processing schemes, namely 1-bit normalization followed by linear stack, 1-bit followed by tf-PWS, RAM normalization followed by linear stack, and RAM followed tf-PWS can be seen in Fig. 3. To assess the best approach, and to monitor the quality of the cross-correlograms, we computed the Signal-to-Noise Ratio (SNR). The SNR is defined as the ratio of the peak amplitude within the signal window and the root mean square (rms) in a noise trailing window (as defined in Bensen et al., 2007). We observed that applying the RAM for time domain normalization and the

tf-PWS to compute the final cross-correlograms produced the highest SNR values. Only cross-correlations having a SNR higher than seven were selected for the following analysis.

As mentioned before, we computed NCFs from a mix of sensors, including the vertical seismometer channel (Z) and the hydrophone (H) for the OBS. The equivalence of the NCFs is illustrated in Fig. 4 a) to d), where we show the EGFs computed between the channels H-Z, H-H, Z-H and Z-Z for the pair OBS04–OBS05. The resulting NCFs display very similar waveforms. However, when the hydrophone is considered the SNR of the computed EGF attains higher values due to lowest amplitude observed in the noise trailing window.

In the investigated frequency band we consider that the EGFs computed from the NCFs are dominated by fundamental mode Rayleigh waves. To measure the group velocity dispersion we measure the maximum energy on group velocity–period diagrams that are computed by applying the S-transform (Stockwell et al., 1996; Schimmel and Gallart, 2005). This maximum energy was used to estimate the group travel time. This transform is similar to filtering the stack of cross-correlograms using narrow-band Gaussian filters (Dziewonski et al., 1969). To account for possible bias produced by changing spectral amplitudes, an instantaneous period was measured at the time of maximum energy and the true period represented in the filtered signal agree to the S-transform centre period.

To transform the group velocity dispersion curves between pairs of stations into a 2D velocity map, for each selected period, we used the group travel time as the input to the 2D tomographic inversion. We used the Fast Marching Surface Tomography code (FMST) (Rawlinson et al, 2005), for performing travel time tomography. Instead of using conventional ray tracing this method computes the travel time of the evolving wave front for each grid point. The group travel times are inverted using the subspace inversion method (Kennett et al., 1988), where the objective function includes smoothing and damping parameters to address the problem of non-uniqueness. Prior to inversion, a checkerboard test, which is discussed in the next section, was applied to define the optimal spatial grid spacing. The 2-D tomographic inversion program outputs the group velocity dispersion in each point of the grid for the different areas of SWIM.

Finally, at each specific point of the grid, well defined in terms of latitude and longitude, the group velocity dispersion was inverted to obtain shear wave velocity profiles as function of depth, using the iterative linearized least-square inversion method of Hermann and Ammon (2007). This algorithm iteratively perturbs a layered velocity model, where we control layers thickness, S-wave velocity, P-wave velocity, density, damping and smoothing, until the best fit between the observed

dispersion measurements and the synthetic dispersion curve is achieved.

## 4. Results

### 4.1 Dispersion measurements

Fig. 5 displays the group velocity-period diagrams obtained from time-frequency analysis for 6 selected station pairs. The dispersion measurements correspond to fundamental-mode Rayleigh waves group velocity in the period band of 4 to 20 seconds. The selected station-to-station paths shown in Fig. 5 illustrate the influence of the presence/absence of sediments and of the transition of seafloor- land- based stations. See Fig. 5a, for location of the station pairs.

Most of the S-Transform diagrams computed for station pairs at the ocean floor exhibit a dispersion branch with group velocities slower than 1 km/s (Fig.5b and c). In the Horseshoe Abyssal plain, the low velocities extend to longer periods suggesting a thicker sedimentary layer than in Horseshoe Valley (Fig. 5c).

Across the Gorringe Bank, OBS01-OBS11 pair, the dispersion curve shows low velocities at shorter periods and rapidly increasing towards longer periods. There is no influence of a thick sedimentary layer, like the one detected in the case of the Horseshoe Abyssal plain and Horseshoe Valley.

The dispersion curve corresponding to the path from the D. Henrique Basin (OBS03) towards PBAR (Barrancos near the Spanish border) display low velocities at shorter periods, smoothly increasing to the longest periods analysed, reflecting the influence of a thicker crust.

Finally, the Rayleigh-wave group measurements obtained for the pairs OBS06-PBDV and PBAR-PFVI are quite similar suggesting that Marques de Pombal Plateau is underlain by continental crust.

### 4.2 Surface wave tomography

For each station pair the obtained group velocities, as a function of period, were transformed into group travel times, as a function of period. These travel times, between each station pair were computed in a 2-D spherical coordinates system, with an uncertainty of  $\pm 0.3$ s due to the location of the OBSs at the seabed. Maps of the group-velocity lateral distributions were obtained using the FMST method (Rawlinson et al. 2005). The dimensions of the grid were chosen based on synthetic checkerboard tests with different grid space sizes. The checkerboard tests are a quick and useful

tool to evaluate the sensitivity of a given data set to resolve velocity structures of given shape, size and amplitude beneath a seismic network. These tests were conducted for several grid sizes in order to estimate the maximum available resolution with the network geometry. Only the ray paths corresponding to the selected group-velocity dispersion measurements were included in the checkerboard test. The input velocity model anomalies had a maximum perturbation of velocity at the nodes of 1.0 km/s. After several trials a grid with a lateral grid spacing of 18.5 km X 18.5 km was adopted. This value was chosen considering the trade-off between the smallest grid node-spacing and the resolution power (Fig.6). Fig. 7 shows, on the top, the ray-path coverage at 8 s. Then it displays the checkerboard results for the periods of 8, 10 and 14s. From the resolution tests, we concluded that the spatial resolution in the centre of the OBSs network is reasonable, due to the high density of crossing paths (c.f. Fig. 7a). However, due to the gap between the seafloor- and land-based stations, we note a decrease in the resolution close to the coastline (Fig. 7b, c and d). The selected grid defines our velocity model on 1080 nodes, which constitutes the inversion grid.

During inversion a bi-cubic B-spline interpolation is applied to produces a continuous, smooth and locally controlled velocity medium. Travel-times are computed for all grid points of the medium. This inversion step allows both smoothing and damping regularization to be imposed in order to address the problem of solution non-uniqueness. When the model perturbations are estimated, the propagation paths are updated and retraced.

Finally, Rayleigh wave group velocity, for periods ranging from 4 to 20 s, are obtained in each velocity node of the inversion grid. The two main parameters that control the locally linearized travel-time inversion are the damping and smoothing factors. The damping factor prevents the solution from becoming unstable, while the smoothing factor constrains the smoothness of the final model. After numerous tests with different sets of these two parameters, we observed that the final models did not show significant differences.

Fig. 8 summarizes the Rayleigh wave group velocities obtained for the periods of 4, 10, 14 and 18 s. The sediment thickness map (Thiebot and Gutscher; 2006) is in Fig.8a displayed for comparison. The 2D maps for the remaining periods can be seen in Fig. S2 of the electronic supplementary material. The group velocities, for the shorter periods, are mostly influenced by the sedimentary layer while the longer periods integrate already the properties of the crust. At the 14 s period, the group velocities are lower where the sediment is thicker (Fig. 8a), namely at the Accretionary Wedge and the Horseshoe Abyssal Plain. The higher group velocities offshore, around 2.2 km/s,

correspond to structural highs like the Gorringe Bank, the Coral Patch Ridge, the Portimão Plateau and the Marques de Pombal Plateau (c.f. Fig. 1a).

In the 14s map (Fig. 8d) the low velocities associated with the Accretionary Wedge correlate well with the ones obtained by Thiebot and Gutscher (2006). At the Horseshoe Abyssal Plain the observed low velocity anomaly are not coherent with the sediment thickness map, probably due to the lack of resolution of the Thiebot and Gutscher (2006) model in this western region. At 18 s, the Gorringe Bank and the D. Henrique basin, correspond to higher velocities, between 2.8 and 3.0 km/s, while the Horseshoe Abyssal Plain and the Accretionary Wedge are still associated with lower Rayleigh group velocities (1.6 to 2.0 km/s). The sensitivity kernels for two areas, Horseshoe Abyssal Plain and Accretionary Wedge, are presented in Fig. S3 of the electronic supplementary material.

### 4.3 S-wave velocity model

To derive a 3-D S-wave velocity model from the attained dispersion Rayleigh wave group velocities for 4-20s in SWIM area, we applied, at each located velocity grid node, an iterative linearized least-square inversion method (Hermann and Ammon; 2007).

In the oceanic domain, the a priori velocity-model for each defined velocity grid node was obtained from previous studies for the SW Iberia (Gonzalez et al., 1996; Gutscher et al., 2002; Sallarès et al., 2011; Sallarès et al., 2013). The first layer is a water column with a  $V_p$  of 1.5 km/s followed by the upper sediments layer with a  $V_p$  of 2.0 km/s, a  $V_p/V_s$  ratio from 1.76 to 1.9 and a density of 1.5 g/cm<sup>3</sup>. The lower sediment layer has a  $V_p$  of 3.8 km/s, a  $V_p/V_s$  ratio of 1.73-1.80 and a density of 2.1 g/cm<sup>3</sup>. The upper, middle and lower crustal layers have a  $V_p$  of, respectively, 5.9, 6.4 and 6.8 km/s, a density ranging from 2.5 to 2.9 g/cm<sup>3</sup> and their  $V_p/V_s$  ratio ranges from 1.72 to 1.83. Finally, the upper mantle has a  $V_p$  of 7.9 km/s, a  $V_p/V_s$  ratio of 1.76 to 1.83 and a density of 3.3 to 3.4 g/cm<sup>3</sup>. For the continental domain, we used the Carrilho et al. (2004) as a priori model with a  $V_p/V_s$  ratio of 1.73. Several tests were carried out with the purpose of inspecting the dependence of the resulting model on the initial model. These tests showed that the perturbations introduced in the starting model did not significantly affect the final  $V_s$  model.

This algorithm iteratively changes a local 1D layered velocity-model. Starting from the a priori model, the depth inversion was performed in several iteration steps, until the best fit between the observed dispersion measurements and the dispersion curve was attained. In the first one, we

inverted for the thickness and in the following ones for the velocity. A fine-tune of the damping and smoothing values was also applied.

For each obtained S-wave velocity model we controlled several output parameters. After several tests which included different combinations of damping and smoothing values we defined that: a) the standard error dispersion fit should be smaller than 0.1 km/s; b) the mean residual dispersion fits lower than 0.05 km/s; c) the average residual dispersion fit lower than 0.08 km/s; d) the signal power fit greater than 99.98% and e) the RMS change in the S-wave velocity model lower than 0.05 km/s. All S-wave velocity models, attained for each grid node, were achieved with values lower or equal to the optimum established values. An example of how the measured Rayleigh group velocities are fitted by the model can be seen in Fig. S4 (in the electronic supplementary material), in each iteration a Vs model is computed and displayed with a different colour line changing from red to blue, where the initial model is red and the accepted final model is blue.

The resulting S-wave velocity model, as a function of depth Below Sea Floor (BSF), is displayed in Fig. 9 for the selected depths 2, 8, 11 and 14 km. The entire set of S-wave velocity maps, namely one map for each km of model, from 1 to 20 km BSF, can be found in Fig. S5, in the electronic supplementary material. The colour scale was chosen to allow an easy identification of the main layers in the derived model: (i) purple corresponds to the upper sedimentary layer and blue the lower sedimentary layer; (ii) green and yellow correspond to the upper and lower crust; (iii) layers in orange or red correspond to the upper mantle.

At shallow depths (2km BSF), in the oceanic domain, the model displays low S-wave velocities, revealing the existence of the sedimentary cover. The S-wave velocity increases slightly from 2 to 8 km depth BSF but the shape of the anomaly is preserved, revealing that the sedimentary layer is thick. Deeper, at 14 km, the S-wave velocity reaches upper mantle values in the oceanic domain while keeping crustal values in the continental margin and onshore. The Gorringe Bank doesn't show a high S-wave anomaly because it is poorly resolved by our dataset with only a single station to the NW of this feature. At 11 km depth BSF the high S-wave velocity anomalies in the Horseshoe Abyssal plain hint to a very thin crust in that area.

The S-wave tomographic model is also explored along six vertical S-wave velocity cross-sections, identified as green lines on Fig. 1b. Two of these lines were chosen to coincide with the deep seismic sounding (DSS) profiles published by Sallarès et al. (2011), Sallarès et al. (2013) and Martínez-Loriente et al. (2014), and can be seen in Fig. 10a and Fig. 10b. The other four of these vertical cross-sections are presented in Fig. 11a)-d).

#### 4.4 Interpretation

The cross-correlation of seismic noise between OBS and land stations allowed for the first time to derive a tomographic image of S-wave velocity for the crust and upper-mantle in SW Iberia. This area has been extensively investigated by MCS providing a detailed image of the sedimentary cover but the deep structure is much less understood. Only two long and properly reversed WAS profiles are available, profile P1 (Martinez-Loriente et al., 2014) and profile P2 (Sallarès et al., 2011) (see location in Fig.1b). Additional information is provided by the revised B/BR profile in Rovere et al. (2004) and by the non-reversed profile IAM-3 in Gonzalez et al. (1996). To make a geological and geophysical interpretation of the new S-wave velocity model we first compare vertical cross-sections with the published results from WAS profiles and then extend the interpretation to the whole area investigated, discussing a series of 4 additional vertical cross-sections. The profile and cross-section location is given in Fig. 1b.

The P-wave velocity models and the coincident S-wave cross section are given in Fig. 10a and 10b for profile P2 (cross-section E-T) and profile P1 (cross-section A-G) respectively. To simplify the comparison between both models the S-wave color code was chosen to be identical to the P-wave code with velocities ratio of 1.76. The poorly constrained areas in the S-wave cross-section are shadowed. This shadowing is replicated in the P-wave velocity model. As mentioned in section 4.2 and Fig.7 the resolution kernel is poor between the seafloor and land based stations, due to the lack of seismic stations in the continental platform, meaning the worst-resolved part of the velocity model corresponding to the distance along profile between 150km and 280km of Fig.10a.

Two main horizons have been interpreted in the S-wave velocity cross-sections, the base of the sedimentary cover and the inferred crust-mantle transition. Profile P2 (Sallarès et al., 2011) and coincident cross-section E-T (Fig. 10a) run approximately North-South (Fig. 1b) and sample the unthinned continental crust of the South Portuguese Zone, the marginal transition domain where continental crust thins to less than 10 km, cross the Ocean-Continent Transition (OCT) and end in the south over oceanic crust of normal thickness and structure (Sallarès et al., 2011). The S-wave velocity model also shows a thick crust on the northern side where the crust-mantle boundary is not found, because it is deeper than 20 km, the deepest depth sampled. Only two crustal layers can be identified, with the upper and mid crustal layers identified by Gonzalez et al. (1998) probably merged in the S-wave model.

The thickening of the sedimentary from North to South is well imaged by the S-wave model, but it exceeds the thickness inferred by the P-wave model in the deeper domains. Between 30 and 100 km the S-wave model shows a very thick layer with velocity similar to sediments, overlying a thin crustal layer. These features are not present in the P-wave model nevertheless constrains well with sediment thickness map of Thiebot and Gutscher (2006) (Fig.8a). However, this section of the P-wave model coincides with a domain that has an anomalous structure when compared to a typical oceanic crust, a thicker layer with velocities lower than 5.5 km/s and a thin layer with velocities greater than 6.5 km/s. We interpret the S-wave model results as a lower resolution image of this transitional domain identified in the P-wave model.

Profile P1 (Martinez-Loriente et al., 2014) and coincident cross-section A-G (Fig. 10b) run approximately NNW-SSE (Fig. 1b). This section starts in the Tagus Abyssal plain in an area poorly resolved by the S-wave model. It crosses the Gorringe Bank, traverses the Horseshoe Abyssal Plain and ends in the Coral Patch Ridge. This profile crosses 3 of the crustal domains as identified by Martinez-Loriente et al. (2014), from NNW to SSE (Fig. 1b), Lower Cretaceous exhumed mantle belonging to the Central Atlantic, Jurassic oceanic crust belonging to the Western Thetys and Jurassic oceanic crust belonging to the Central Atlantic.

The comparison of S-wave and P-wave velocity models show that in these deep water domains the S-wave model gives a thicker sedimentary cover. This is particularly evident in the top of the Gorringe Bank but we must remark that, without any OBS placed close by, this area is poorly defined by the S-wave model. The basement relief, however, is well recovered by the S-wave model. The small lateral differences seen between both models can be ascribed to the lower horizontal resolution of the S-wave model. The variable thickness of the crust, or the layer with crustal velocities, is also well recovered by the S-wave model. At the Gorringe Bank area these crustal velocities are interpreted as being the result of extensive and deep penetration serpentinization of the mantle (Martinez-Loriente et al., 2014, Sallarès et al., 2013). The Horseshoe Abyssal plain is shown to be (in both models) underlain by very thin oceanic crust or serpentinized upper-mantle, while the Coral Patch Ridge shows, in both models, normal (S-wave) or slightly thinned (P-wave) oceanic crust.

The analysis of coincident P- and S-wave cross-sections showed that the S-wave model derived in this work provides reliable estimates on the basement relief and on the variations of thickness of the crust or layers with crustal velocities. In the deep water particularly the S-wave model provides an excessive estimate on the sedimentary cover thickness. Due to the differences in horizontal

resolution between both models, the S-wave features are sometimes slightly displaced in relation to the same features seen in the P-wave model.

We have also examined the S-wave tomographic model along 4 additional cross-sections (Fig. 11a to 11d), which location was given in Fig. 1b.

Cross-section H-D (Fig. 11a), with a direction WSW-ENE starts at the western tip of the Central Atlantic Jurassic oceanic crust domain and ends in the thinned continental crust domain, as defined by Martinez-Loriente et al. (2014). We observed a thickening of the sedimentary cover in the deep-water areas, but the estimated thicknesses are likely to be in excess. The thinned continental crust domain is well imaged in the ENE, after km 140 in the model. The oceanic crust domain, however, seems to be underlain by anomalous thin oceanic crust or serpentinized upper mantle. The crustal structure is to the one found in the Horseshoe Abyssal Plain, discussed in Fig. 10b.

Cross-section A-B (Fig. 11b), with a direction NW-SE, is similar to profile P1 discussed above. It also starts in the Tagus Abyssal (an area poorly resolved by the S-wave model), crosses the Gorringe Bank, traverses the Horseshoe Abyssal Plain (HAP) and ends in Horseshoe Valley (Fig. 1a, 1b) which is presumed to be underlain by Jurassic oceanic crust belonging to the Western Thetys (Martinez-Loriente et al., 2014). The S-wave model shows a thick layer at the Gorringe Bank and NW HAP with velocities that are interpreted as representing a thick layer of exhumed and altered upper mantle. The S-wave model, SE of km 100, shows a thin layer with crustal velocities, beneath a thick pile of sediments (with a thickness likely to be in excess). As for the H-D cross-section we interpret this domain as representing anomalous thin oceanic crust or serpentinized upper mantle.

Cross-section I-F (Fig. 11c) runs SW-NE along the SE side of the Gorringe Bank, in the Horseshoe Abyssal Plain. The S-wave model shows a sedimentary cover and a layer with crustal velocities with variable thicknesses. Considering that this section crosses profile P1, we interpret this crustal structure as representing a layer of exhumed upper mantle with a great variation in the degree and penetration of serpentinization.

Cross-section G-F (Fig. 11d) runs S-N from the Coral Patch Ridge across the Horseshoe Abyssal Plain ending at the Marquês de Pombal plain, East of the Gorringe Bank (Fig. 1a, 1b). The S-wave model shows that the Coral Patch is underlain by oceanic crust with normal thickness (between 0 and 30 km in the model). In the Horseshoe Abyssal Plain a considerable thickening of the sedimentary cover is shown. North of 30 km the S-wave model shows an anomalous thin oceanic

crust. These velocities may also be interpreted as representing altered upper mantle without any crustal layer. When the profile crosses from the Western Thetys domain of Jurassic oceanic crust to the Lower Cretaceous exhumed mantle, as proposed by Martinez-Loriente et al. (2014) we do not see any change in crustal thickness, only a change in the basement depth, being shallower to the North.

## 5. Conclusions

Cross-correlation of one-day length ambient noise records, over eleven months, allowed retrieving EGF's with good SNR. The dispersion analysis of Rayleigh wave resulting in the evaluation of group velocities between stations-pairs for a selection of representative periods. After regularization the group velocities on each grid point were inverted as a function of depth to obtain the first 3D shear-wave velocity model for SW Iberia combining seafloor- and land- based data. The size of the grid cells was defined from a checkerboard test.

Taking advantage that OBSs also recorded the hydrophone channel, the tests performed between all pairs of components (Z and H) showed that it was possible to retrieve propagation properties of seismic waves along paths between ocean and land stations with a mix of hydrophones and seismometers cross-correlations. Furthermore the hydrophone-seismometer cross-correlations showed better SNR when compare with the same path seismometer-seismometer cross-correlation.

Another significant achievement was the enhancement of the temporal and spatial randomization of ambient seismic noise sources with the tf-PWS methodology that attenuates the incoherent noise. Thus, dispersion velocities for the different paths and sensors were obtained which allowed a joint inversion of data from OBSs and land stations.

Three main layers could be identified on the 3D S-wave velocity model: i) the sedimentary cover; ii) a layer with velocities that could represent continental crust, oceanic crust, or exhumed and serpentinized upper mantle; iii) upper mantle. The structure inferred from the S-wave model was compared with the previously known geophysical and geological information. We verified that variations in sedimentary thickness and basement relief were well represented but the S-wave model provided an estimate in excess to the known values along control profiles. These differences were particularly seen in the deeper areas of the investigated area but nearly absent close to the continental margin where sediment is thinner.

The comparison between the S-wave model and two P-wave velocity profiles obtained from the inversion of refraction and wide-angle reflection seismic data showed that the 3D model reproduced quite well the variations in thickness of the layer (ii) in all the domains investigated. Extending this interpretation to the analysis of 4 other model cross-sections clearly suggests that West of profile P2 (Fig. 1b) the Horseshoe Valley (HV) and Horseshoe Abyssal Plain are underlain by either anomalously thin oceanic crust or by exhumed and serpentinized upper mantle. This conclusion questions the limits of crustal domains as proposed by Martinez-Loriente et al. (2014) that suggested that the HV should be underlain by (normal) oceanic crust of Jurassic age belonging to the Western Thetys. Gonzalez et al. (1996) based on non-reversed refraction seismic data and gravity modelling already suggested that the HV has a very thick sedimentary cover underlain by a crustal layer of ~5 km thickness. Also profile B/BR presented by Purdy (1975) and revised by Rovere et al. (2004) with shot B at the corner between 3 of the zones identified by Martinez-Loriente et al. (2014) and shot BR in the Jurassic oceanic crust domain of the Western Thetys (Fig. 1b) showed that side B as a less than normal crust underlain by anomalous low velocity mantle, while side BR has a much thinner crust with the same anomalous mantle. All this information taken together indicates that the Horseshoe Valley from the Horseshoe Fault to profile P2 is underlain mostly by anomalous oceanic crust and/or exhumed and altered mantle. Profile P2 may be located at the transition to normal oceanic crust, to the East. This peculiar location of profile P2 may explain the largest discrepancy we found between P- and S-wave velocity models. With a lower horizontal resolution, the S-wave model may be capturing the influence of the anomalous crustal structure just west of the cross-section (Fig. 10a).

The results obtained regarding the deep structure of the Southwest Iberian margin show that ambient noise tomography could be a reasonable tool to get an integrated image of onshore, offshore and marginal domains but needs a geometry including OBSs near shore.

## Acknowledgements

This article is a contribution of projects NEAREST FP6-2005-GLOBAL-4 (OJ 2005 C177/15), QuakeLoc-PT (PTDC/GEO-FIQ/3522/2012), AQUAREL (PTDC/CTE-GIX/116819/2010), WILAS (PTDC/CTE-GIX/097946/2008). The publication is supported by FCT through project UID/GEO/50019/2013 - Instituto Dom Luiz.

## References

- Banda, E., M. Torne, and the IAM Group, 1995. Iberian Atlantic margins group investigates deep structure of ocean margins, a multichannel seismic survey. *EOS* 76(3), 25-29.
- Baptista, M. A., and J. M. Miranda, 2009. Revision of the Portuguese catalog of tsunamis, *Nat. Hazards Earth Syst. Sci.* 9, 25-42. doi: 10.5194/nhess-9-5-2009.
- Bensen, G.D., Ritzwoller, M.H., Barmin, M.P., Levshin, A.L., Lin, F., Moschetti, M.P., Shapiro, N.M. and Yang, Y., 2007. Processing seismic ambient noise data to obtain reliable broad-band surface wave dispersion measurements. *Geophys. J. Int.* 169, 1239-1260.
- Bonnin, J., Olivet, J. L. and Auzende, J.M., 1975. Structure en nappe a l'ouest de Gibraltar. *C. R. Academy of Science* 280(5), 559-562.
- Bowden, D. C., M. D. Kohler, V. C. Tsai, and D. S. Weeraratne, 2016. Offshore Southern California lithospheric velocity structure from noise cross-correlation functions. *Journal Geophys. Res.: Solid Earth*, 121. doi: 10.1002/2016JB012919.
- Campillo, M. and Paul, A., 2003. Long-range correlations in the diffuse seismic coda. *Science* 299, 547-549. doi: 10.1126/science.1078551.
- Carrilho, F., Teves-Costa, P., Morais, I., Pagarete, J. and Dias, R., 2004. GEOALGAR Project: First Results on Seismicity and Fault-plane Solutions. *Pure Appl. Geophysics* 161, 589-606. doi: 10.1007/s00024-003-02464-3.
- Contrucci, I., Klingelhoefer, F., Perrot, J., Bartolome, R., Gutscher, M.-A., Sahabi, M., Malod, J., Rehault, J.-P., 2004. The crustal structure of the NW-Moroccan continental margin from wide-angle and reflection seismic data. *Geophysical Journal International* 159, 117–128. doi: 10.1111/j.1365-246X.2004.02391.x
- DeMets, C., R. G. Gordon, and D. F. Argus, 2010. Geologically current plate motions. *Geophys. J. Int.* 181, 1-80. doi: 10.1111/j.1365246X.2009.04491.x.

- Dias, R. C., Julià, J. and Schimmel, M., 2015. Rayleigh-Wave, Group-Velocity tomography of the Borborema Province, NE Brasil, from ambient seismic noise. *Pure Appl. Geophysics* 172, 1429-1449. doi: 10.1007/s00024-014-0982-9.
- Duarte, J.C., Rosas, F.M., Terrinha, P., Schellart, W.P., Boutelier, D., Gutscher, M.A., Ribeiro, A., 2013. Are subduction zones invading the Atlantic? Evidence from the SW Iberia margin. *Geology*. doi: 10.1130/G34100.1.
- Dziewonski, A., Bloch, S., and Landisman, M., 1969. A technique for analysis of transient seismic signals. *Bull. Seism. Soc. Am.* 59(1), 427-444.
- Geissler, W.H., Matias, L., Stich, D., Carrilho, F., Jokat, W., Monna, S., IbenBrahim, A., Mancilla, F., Gutscher, M.A., Sallarès, V. and Zitellini, N., 2010. Focal mechanisms for sub-crustal earthquakes in the Gulf of Cádiz from a dense OBS deployment. *Geophysical Research Letters* 37, L18309. doi: 10.1029/2010GL044289.
- González, A., Torne, M., Córdoba, J., Vidal, N., Matias, L. and Diaz, J., 1996. Crustal Thinning in the Southwestern Iberian Margin. *Geophys. Res. Letters*. 23, 2477-2480.
- González, A., Córdoba, D. and Matias, L.M., 1998. Seismic crustal structure in the southwest of the Iberian Peninsula and Gulf of Cadiz. *Tectonophysics* 296(3-4), 317-331.
- Gràcia, E., Dañobeitia, J., Vergés, J., Bartolomé, R., 2003a. Crustal architecture and tectonic evolution of the Gulf of Cádiz (SW Iberian margin) at the convergence of the Eurasian and African plates. *Tectonics* 22(4), 1033. doi: 10.1029/2001TC901045.
- Gràcia, E., Danobeitia, J., Vergés, J., Cordoba, D., PARSIFAL Team, 2003b. Mapping active faults offshore Portugal (36°N–38°N): implications seismic hazard assessment along the southwest Iberian margin. *Geology* 31(1), 83-86.

- Gutscher, M.A., Malod, J., Rehault, J.-P., Contrucci, I., Klingelhoefer, F., Mendes-Victor, L., Spakman, W., 2002. Evidence for active subduction beneath Gibraltar. *Geology* 30(12), 1071-1074.
- Gutscher, M.A., Dominguez, S., Westbrook, G.K., Gente, P., Babonneau, N., Mulder, T., Gonthier, E., Bartolome, R., Luis, J., Rosas, F., Pedro, T., the Delila and DelSis Scientific Teams, 2009. Tectonic shortening and gravitational spreading in the Gulf of Cadiz accretionary wedge: observations from multi-beam bathymetry and seismic profiling. *Mar. Petrol. Geol.* 26, 647-659.
- Gutscher, M.A., Dominguez, S., Westbrook, G.K., Gente, P., Leroy, P., 2009. Deep structure, recent deformation and analog modeling of the Gulf of Cadiz accretionary wedge: Implications for the 1755 Lisbon earthquake. *Tectonophysics* 475, 85-97. doi: 10.1016/j.tecto.2008.11.031.
- Gutscher, M.A., Dominguez, S., Westbrook, G.K., Le Roy, P., Rosas, F., Duarte, J.C., Terrinha, P., Miranda, J.M., Graindorge, D., Gailler, A., Sallares, V., 2012. The Gibraltar subduction: A decade of new geophysical data. *Tectonophysics* 574-575, 72-91.
- Haned, A., Stutzmann, E., Schimmel, M., Kiselev, S., Davaille, A., and Yelles-Chaouche, A., 2016. Global tomography using seismic hum. *Geophys. J. Int.* 204, 1222-1236. doi: 10.1093/gji/ggv516.
- Harmon, N., Forsyth, D. and Spahr Webb, 2007. Using Ambient Seismic Noise to Determine Short-Period Phase Velocities and Shallow Shear Velocities in Young Oceanic Lithosphere. *Bulletin of the Seismological Society of America* 97 (6), 2009-2023. doi: 10.1785/0120070050.
- Hasselmann, K., 1963. A statistical analysis of the generation of microseisms. *Rev. Geophys.* 1, 177-209.
- Herrmann, R. B. and C. J. Ammon, 2007. Computer Programs in Seismology version 3.30: Surface Waves, Receiver Functions and Crustal Structure. St. Louis University, Missouri (2002).

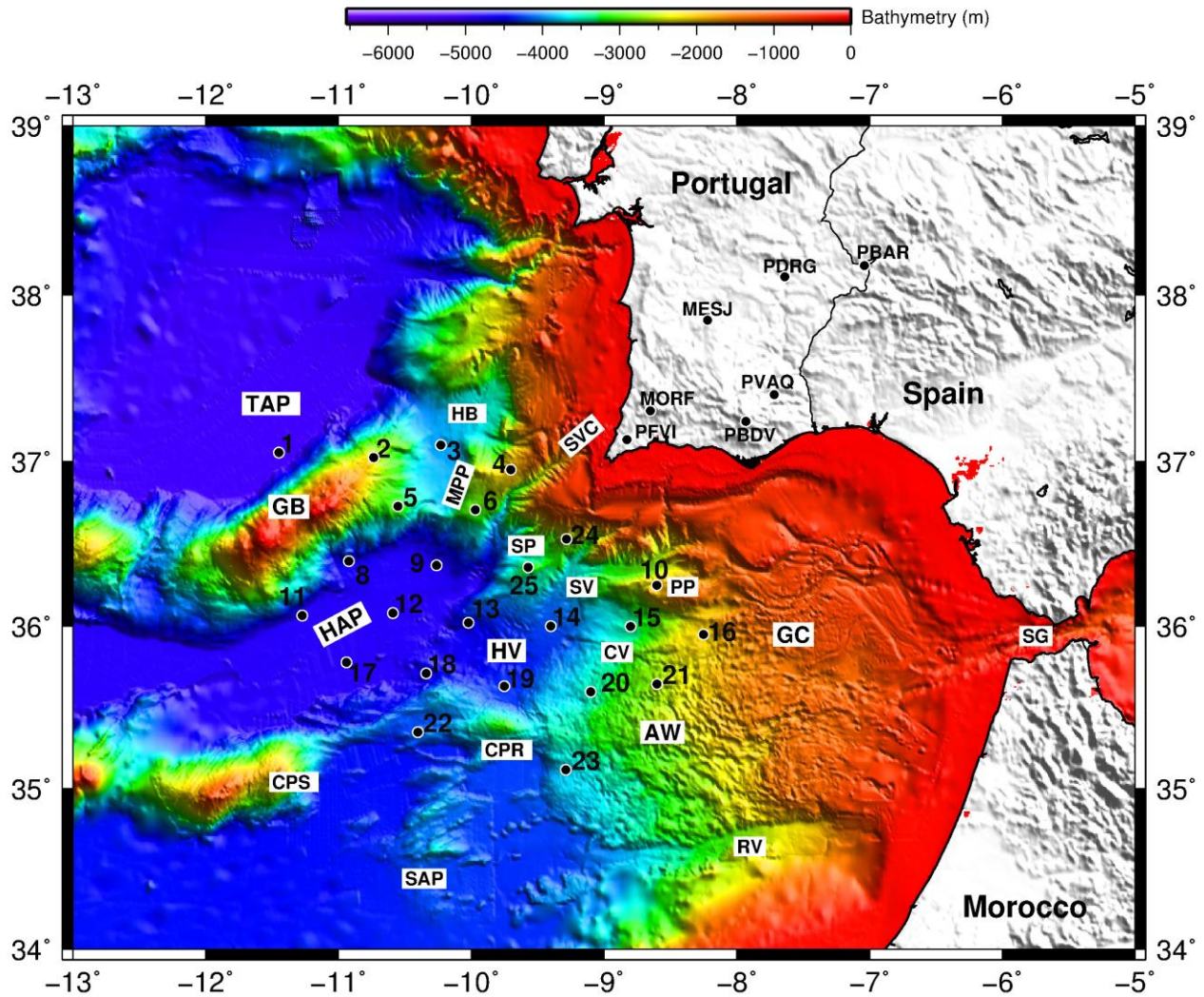
- ILIHA-DSS Group (reporters: J. Diaz, J. Gallart, D. Córdoba, L. Senos, L. Matias, E. Suriñach, A. Him and P. Maguire), 1993. A deep seismic sounding investigation of lithospheric heterogeneity and anisotropy beneath the Iberian Peninsula, ed: J. Badal, J. Gallart e H. Paulssen (editores), Seismic Studies of the Iberian Peninsula. Tectonophysics 222, 35-51.
- Julivert, M., Fontboté, J.M., Ribeiro, A. and Conde, L.N., 1972. Memoria explicativa del mapa tectónico de la Península Ibérica y Baleares, Inst. Geol. y Min. de Esp.
- Jaffal, M., Klingelhofer, F., Matias, L., Teixeira, F., Amrhar, M., 2009. Crustal structure of the NW Moroccan margin from deep seismic data (SISMAR Cruise). Compt. Rendus Geosci. 341 (6), 495–503.
- Kennett, B.L.N., Sambridge, M.S., and Williamson, P.R., 1988. Subspace methods for large scale inverse problems involving multiple parameter classes. Geophysical Journal 94, 237-247.
- Klingelhofer Frauke, Biari Youssef, Sahabi Mohamed, Aslanian Daniel, Schnabel Michael, Matias Luis, Benabdellouahed Massinissa, Funck Thomas, Gutscher Marc-Andre, Reichert Christian, Austin James A., 2016. Crustal structure variations along the NW-African continental margin: a comparison of new and existing models from wide-angle and reflection seismic data. Tectonophysics 674, 227-252. doi : 10.1016/j.tecto.2016.02.024
- Lobkis, O. I. and Weaver, R.L., 2001. On the emergence of the Green's function in the correlations of a diffuse field. J. acoust. Soc. Am. 110, 3011-3017.
- Longuet-Higgins, M. S., 1950. A theory of the origin of micro-seisms. Philos. Trans. R. Soc. London, Ser. A 243, 1-35.
- Martinez-Loriente, S., V. Sallarès, E. Gràcia, R. Bartalome, J. J. Dañobeitia and N. Zitellini, 2013. Active deformation in old oceanic lithosphere and significance for earthquake hazard: Seismic imaging of the Coral Patch Ridge area and neighboring abyssal plains (SW Iberian Margin). Geochem. Geophys. Geosyst. 14, 2206-2231. doi: 10.1002/ggge.20173.

- Martinez-Loriente, S., V. Sallarès, E. Gràcia, R. Bartalome, J. J. Dañobeitia and N. Zitellini, 2014. Seismic and gravity constraints on the nature of the basement in the Africa-Eurasia plate boundary: New insights for the geodynamic evolution of the SW Iberian margin. *J. Geophysics Res. Solid Earth* 119, 127-149. doi: 10.1002/2013JB010476.
- Matos, C., Silveira, G., Matias, L., Caldeira, R., Ribeiro, M. L., Dias, N., Kruger, F., Bento dos Santos, T., 2014. Upper crustal structure of Madeira Island revealed from ambiente noise tomography. *Journal of Volcanology and Geothermal Research* 298, 136-145. doi: 10.106/j.jvolgeores.2015.03.17.
- Nocquet, J. M., and E. Calais, 2004. Geodetic measurements of crustal deformation in the Western Mediterranean and Europe. *Pure Appl. Geophys.* 161, 661-681.
- Platt, J. and Houseman, G., 2003. Evidence for active subduction beneath Gibraltar: Comment and Reply: COMMENT. *Geology* 31, E22.
- Purdy, G. M., 1975. The eastern end of the Azores-Gibraltar plate boundary. *Geophys. J. R. Astron. Soc.* 43, 123-150.
- Rawlinson, N., Sambridge, M., 2005. The fast marching method: An effective tool for tomographic imaging and tracking multiple phases in complex layered media. *Explor. Geophysics* 36, 341-350.
- Ribeiro, A., Quesada, C. and Dallmeyer, R. D., 1990. Geodynamic evolution of the Iberian Massif, in: *PreMesozoic Geology of Iberia*, 299-409, R. D. Dallmeyer e E. Martinez Garcia eds., Springer-Verlag, Berlin, Heidelberg, New York.
- Rovere, M., Ranero, C.R, Sartori, R., Torelli, L. and Zitellini, N., 2004. Seismic images and magnetic signature of Late Jurassic to Early Cretaceous Africa-Eurasia plate boundary off SW Iberia. *Geophys. J. Int.* 158, 554-568.

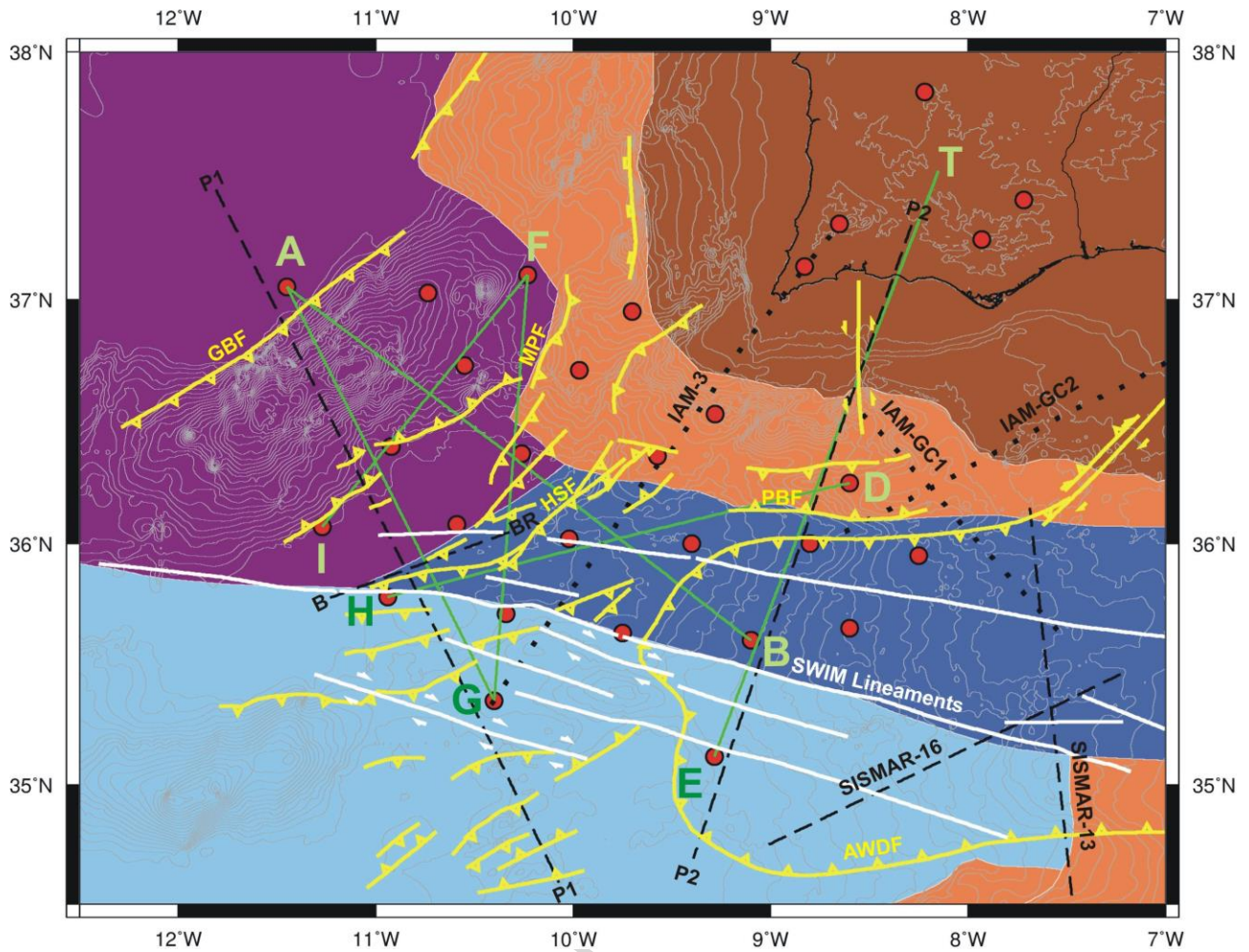
- Sabra, K. G., Gerstoft, P., Roux, P., Kuperman, W. A. and Fehler, M., 2005a. Extracting time-domain Green's function estimates from ambient seismic noise. *Geophysical Research Letters* 32, L03310. doi: 10.1029/2004GL021862.
- Sabra, K.G., Gerstoft, P., Roux, P., Kuperman, W.A. and Fehler, M., 2005b. Surface wave tomography from seismic ambient noise in Southern California, *Geophys. Res. Lett.* 32, L14311. doi: 10.1029/2005GL023155.
- Sallarès, V., Gailler, A., Gutscher, M. A., Graindorge, D., Bartolome, R., Gràcia, E., Díaz, Jordi, Dañobeitia, J.J., Zitellini, N., 2011. Seismic evidence for the presence of Jurassic oceanic crust in the central Gulf of Cadiz (SW Iberian margin). *Earth and Planetary Science Letters* 311, 112-123. doi: 10.1016/j.epsl.2011.09.003.
- Sallarès, V., Lorient, S.M., Prada, M., Gràcia, E., Ranero, C., Gutscher, M. A., Bartolome, R., Gailler, A., Dañobeitia, J.J., Zitellini, N., 2013. Seismic evidence of exhumed mantle rock basement at the Gorringe bank and the adjacent horseshoe and Tagus abyssal plains (SW Iberia). *Earth and Planetary Science Letters* 365, 120-131. doi: 10.1016/j.epsl.2013.01.021.
- Sartori, R., Torelli, L., Zitellini, N., Peis, D., Lodolo, E., 1994. Eastern segment of the Azores–Gibraltar line (central–eastern Atlantic): an oceanic plate boundary with diffuse compressional deformation. *Geology* 22, 555-558.
- Schimmel, M., Paulssen, H., 1997. Noise reduction and detection of weak, coherent signals through phase-weighted stacks. *Geophys. J. Int.* 130, 497-505. doi: 10.1111/j.1365-246X.1997.tb05664.x.
- Schimmel, M., Gallart, J., 2005. The Inverse S-transform in filters with time-frequency localization. *IEEE Transactions on signal processing* 53, 11, 4417-4422. doi: 10.1109/TSP.2005.857065.
- Schimmel, M. and Gallart, J., 2007. Frequency-dependent phase coherence for noise suppression in seismic array data. *J. Geophys. Res.* 112, B04303. doi: 10.1029/2006JB004680.

- Schimmel, M., Stutzmann, E., Arduin, F., Gallart, J., 2011. Polarized Earth's Ambient Microseismic Noise. *Geochem. Geophys. Geosyst.*, 12, Q07014. doi:10.1029/2011GC003661.
- Shapiro, N. M., and Campillo, M., 2004. Emergence of broadband Rayleigh waves from correlations of the ambient seismic noise. *Geophys. Res. Lett.* 31, L07614. doi: 10.1029/2004GL019491.
- Shapiro, N., Campillo, M., Stehly, L. and Ritzwoller, M. H., 2005. High-Resolution Surface-Wave Tomography from Ambient Seismic Noise. *Science* 307, 1615-1618.
- Silveira, G., Dias, N. A. and Villaseñor, A., 2013. Seismic imaging of the Western Iberian crust using ambient noise: Boundaries and internal structure of the Iberian Massif. *Tectonophysics* 589, 186-194.
- Snieder, R., 2004. Extracting the Green's function from the correlation of coda waves: a derivation based on stationary phase. *Phys. Rev. E.* 69(4), 046610. doi: 10.1103/PhysRevE.69.046610.
- Stich, D., R. Martin, and J. Morales, 2010. Moment tensor inversion for Iberia-Maghreb earthquakes 2005–2008. *Tectonophysics* 483, 390-398. doi: 10.1016/j.tecto.2009.11.006.
- Stockwell, R.G., Mansinha, L., and Lowe, R.P., 1996. Localization of the complex spectrum: The S-transform. *IEEE Trans. Signal Process* 44, 998-1001.
- Terrinha, P., Pinheiro, L.M., Henriët, J.-P., Matias, L., Ivanov, M.K., Monteiro, J.H., Akhmetzhanov, A., Volkonskaya, A., Cunha, T., Shaskin, P., Rovere, M., the TTR10 Shipboard Scientific Party, 2003. Tsunamigenic-seismogenic structures, neotectonics, sedimentary processes and slope instability on the southwest Portuguese Margin. *Mar. Geol.* 195, 55-73.
- Terrinha, P., Matias, L., Vicente, J., Duarte, J., Luís, J., Pinheiro, L., Lourenço, N., Díez, S., Rosas, F., Magalhães, V., Valadares, V., Zitellini, N., Mendes Víctor, L., MATESPRO Team, 2009. Morphotectonics and strain partitioning at the Iberia-Africa plate boundary from multibeam and seismic reflection data. *Mar. Geol.* 267, 156-174.

- Thiebot, E. and M. A. Gutscher, 2006. The Gibraltar Arc seismogenic zone (part 1): Constraints on a shallow east dipping fault plane source for the 1755 Lisbon earthquake provided by seismic data, gravity and thermal modeling. *Tectonophysics* 426, 135–152. doi: 10.1016/j.tecto.2006.02.024.
- Torelli, L., R. Sartori, and N. Zitellini, 1997. The giant chaotic body in the Atlantic Ocean off Gibraltar: New results from a deep seismic reflection survey. *Mar. Pet. Geol.* 14, 125-138.
- Tortella, D., Torné, M., Pérez-Estáun, A., 1997. Geodynamic Evolution of the Eastern Segment of the Azores–Gibraltar Zone: the Gorringe Bank and the Gulf of Cadiz Region. *Marine Geophysical Researches* 19, 211-230.
- Zha, Y., Webb, S.C., Wei, S.S., Wiens, D.A., Blackmann, D.K., Menke, W., Dunn, R.A., and Conder, J. A., 2014. Seismological imaging of ridge-arc interaction beneath the Eastern Lau Spreading Center from OBS ambient noise tomography. *Earth and Planetary Science Letters* 408,194-206.
- Zitellini, N., Mendes, L. A., Cordoba, D., Danobeitia, J., Nicolich, R., Pellis, G., Ribeiro, A., Sartori, R., Torelli, L., Bartolomé, R., Bortoluzzi, G., Calafato, A., Carrilho, F., Casoni, L., Chierici, F., Corela, C., Correggiari, A., Della Vedova, B., Gràcia, E., Jornet, P., Landuzzi, M., Ligi, M., Magagnoli, A., Marozzi, G., Matias, L., Penitenti, D., Rodriguez, P., Rovere, M., Terrinha, P., Vigliotti, L., Zahinos Ruiz, A., 2001. Source of 1755 Lisbon Earthquake and Tsunami Investigated. *Eos Trans. AGU* 82(26), 285, 290-291.
- Zitellini, N., Rovere, M., Terrinha, P., Chierici, F.,Matias, L., BIGSETS Team, 2004. Neogene through Quaternary tectonic reactivation of the SW Iberian passive margin. *Pure and Applied Geophysics* 161, 565-587.
- Zitellini, N., Gracia, E., Matias, L., Terrinha, P., Abreu, M.A., DeAlteriis, G., Henriët, J.P., Dañobeitia, J.J., Masson, D.G., Mulder, T., Ramella, R., Somoza, L., Diez, S., 2009. The quest for the Africa–Eurasia plate boundary west of the Strait of Gibraltar. *Earth and Planetary Science Letters* 280(1–4), 13-50.



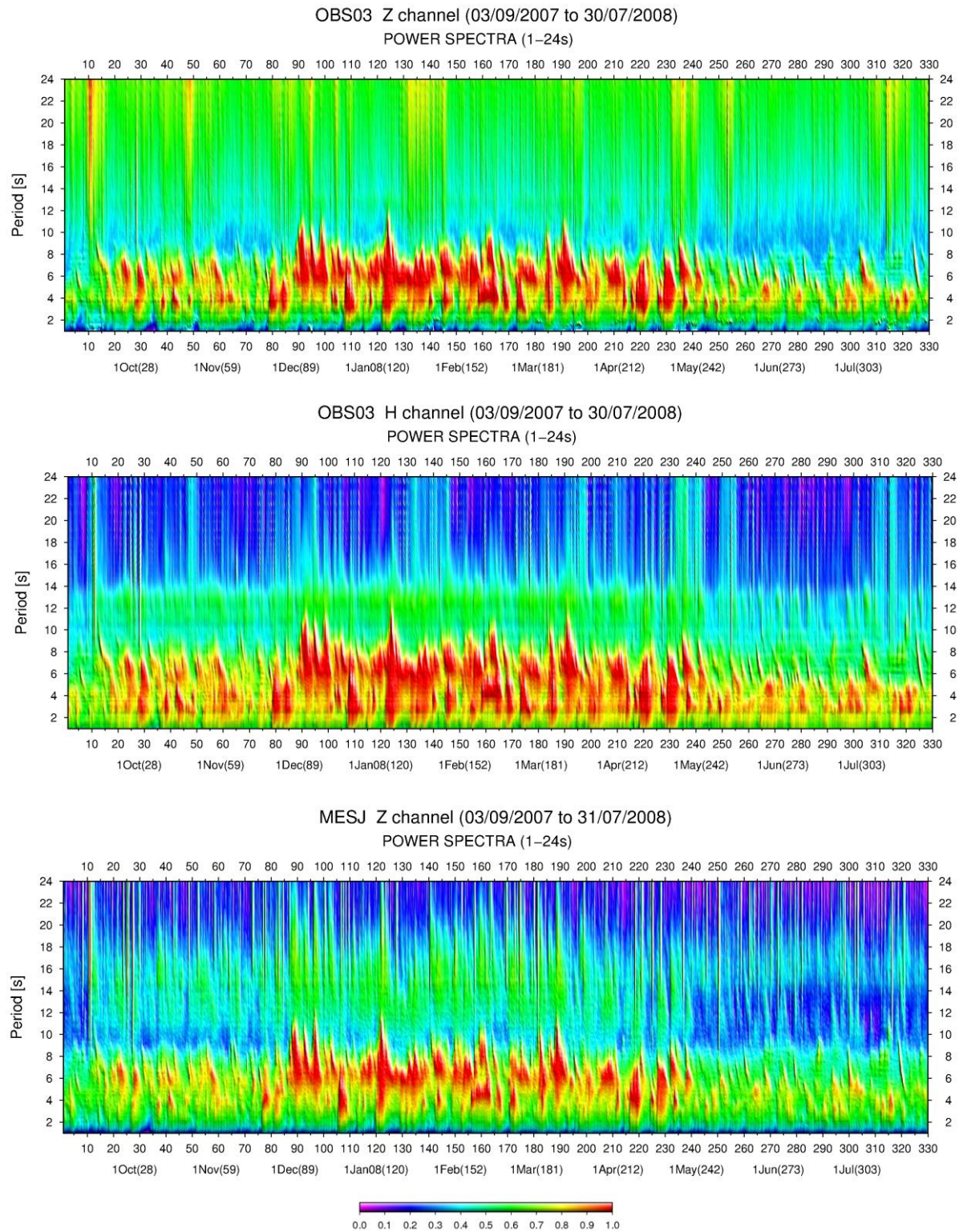
**Fig. 1. a)** Presentation of the study area and location of the seven land stations and 24 OBS (1 represents OBS01, and so on) used in this study. Background bathymetry and topography from [http://w3.ualg.pt/%7Ejluismirone/misc/bat\\_atl\\_30c\\_j.grd.zip](http://w3.ualg.pt/%7Ejluismirone/misc/bat_atl_30c_j.grd.zip). Main geographical features shown: TAP – Tagus Abyssal Plain; HB – D. Henrique Basin; GB Gorringer Bank; MPP – Marquês de Pombal Plateau; SVC – São Vicente Canyon; SP – Sagres Plateau; HAP – Horseshoe Abyssal Plain; SV – Sagres Valley; PP – Portimão Plateau; HV – Horseshoe Valley; CV – Cadiz Valley; GC – Gulf of Cadiz; SG – Strait of Gibraltar CPR – Coral Patch Ridge; AW – Accretionary Wedge; CPS – Coral Patch Seamounts; SAP – Seine Abyssal Plain; RV – Rharb Valley.



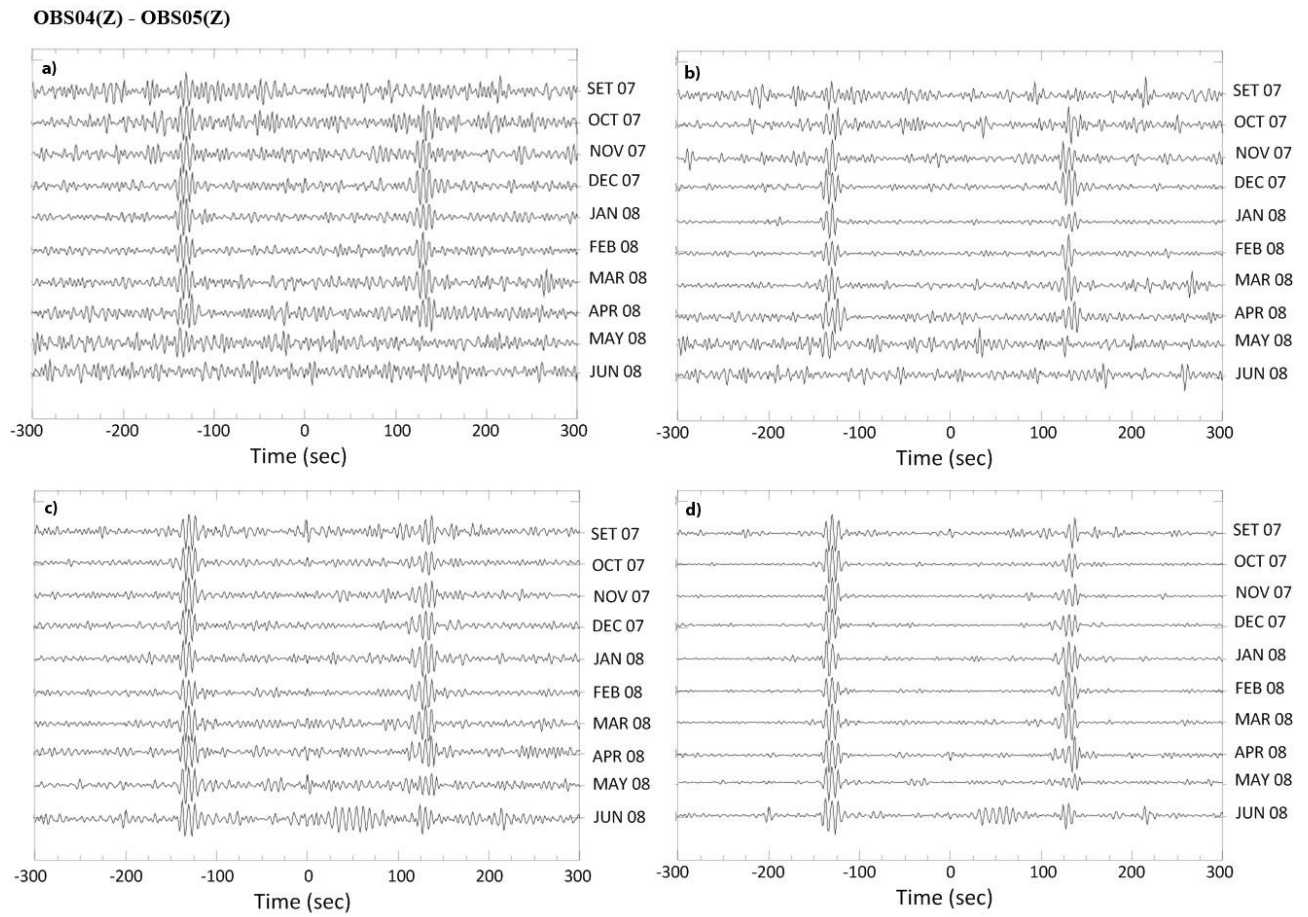
**Fig. 1. b)** Geological setting of the investigated area. Red dots show the location of OBS and land stations. The tectonic features in the offshore are a simplified version of Duarte et al. (2013) (no distinction is done for blind faults or probable faults). Yellow – active or most probably active faults and the deformation front of the accretionary wedge (AWDF). White – the active SWIM lineaments with right lateral slip movement. The deep crustal structure has been investigated by refraction and wide-angle reflection seismic profiles in black. Dashed lines show profiles that are controlled by sensors in the ocean and thus are properly reversed: P2 - Sallares et al. (2011); P1 – Sallares et al. (2013), Martinez-Loriente et al. (2014); Sismar-16 – Gutscher et al. (2001); SISMAR-13 – Thiebot et al. (2005), revised by Klingelhoefer et al. (2016); B/BR – Purdy (1975), revised by Rovere et al. (2004). Dotted lines are wide-angle reflection profiles investigated only by land stations: IAM-3 – Gonzalez et al. (1996); IAM-GC1 and IAM-GC2 - Gonzalez et al. (2001). The colour background represents the crustal domains proposed by Martinez-Loriente et al. (2014): dark shade of blue – Jurassic oceanic crust belonging to the Western Thetys; light blue - Jurassic oceanic crust belonging to the Central Atlantic; purple – Lower Cretaceous exhumed mantle belonging to the North Atlantic; orange and brown – continental crust, thinned along the margins. The main

tsunamigenic faults identified are: GBF – Gorrige Bank fault; HSF – Horseshoe Fault; MPF – Marquês de Pombal fault; PBF – Portimão Bank fault. AWDF = Accretionary wedge deformation front. Green letters and lines show the location of the S-wave model cross-sections to be discussed in Figs. 9 and 10.

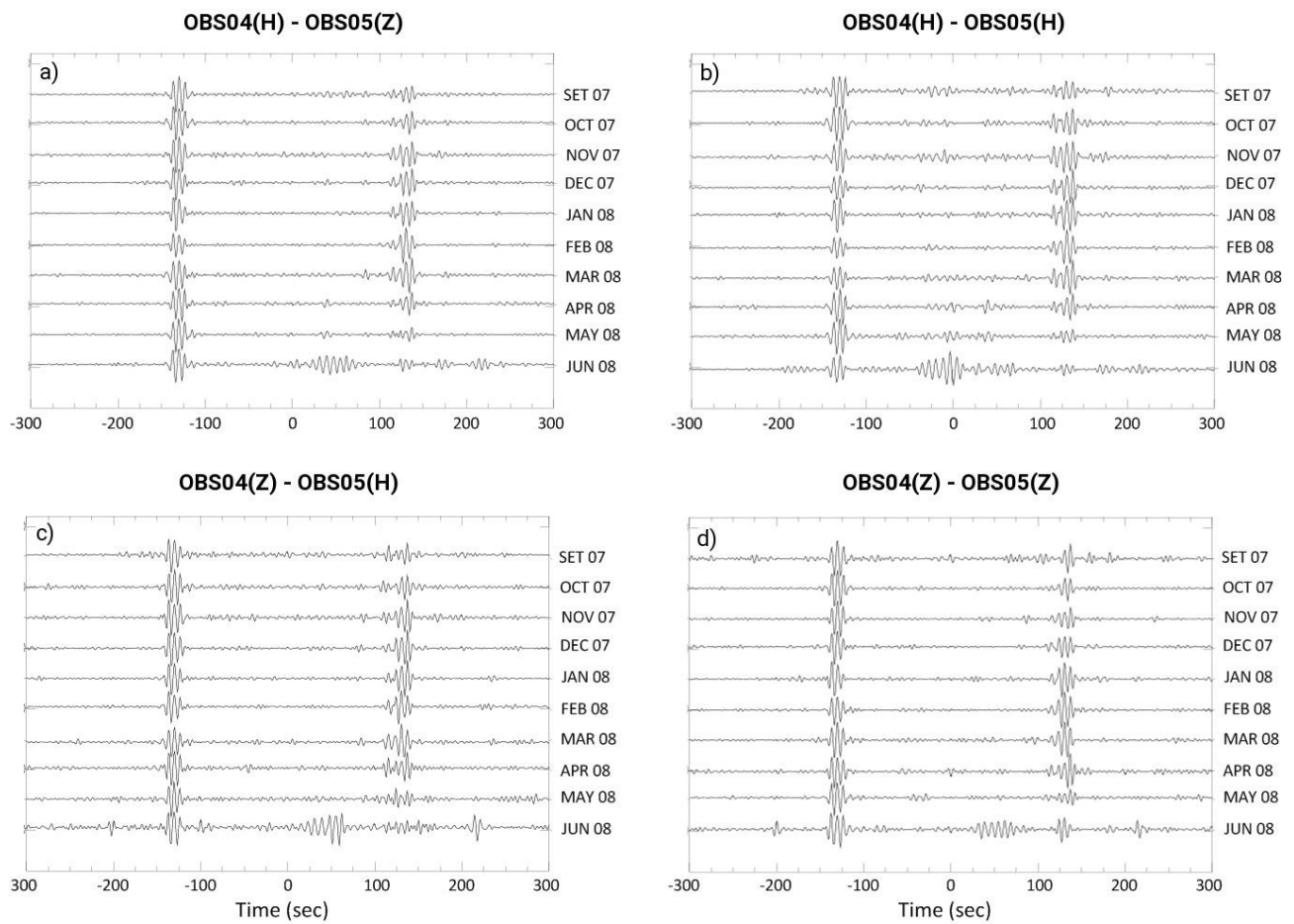
ACCEPTED MANUSCRIPT



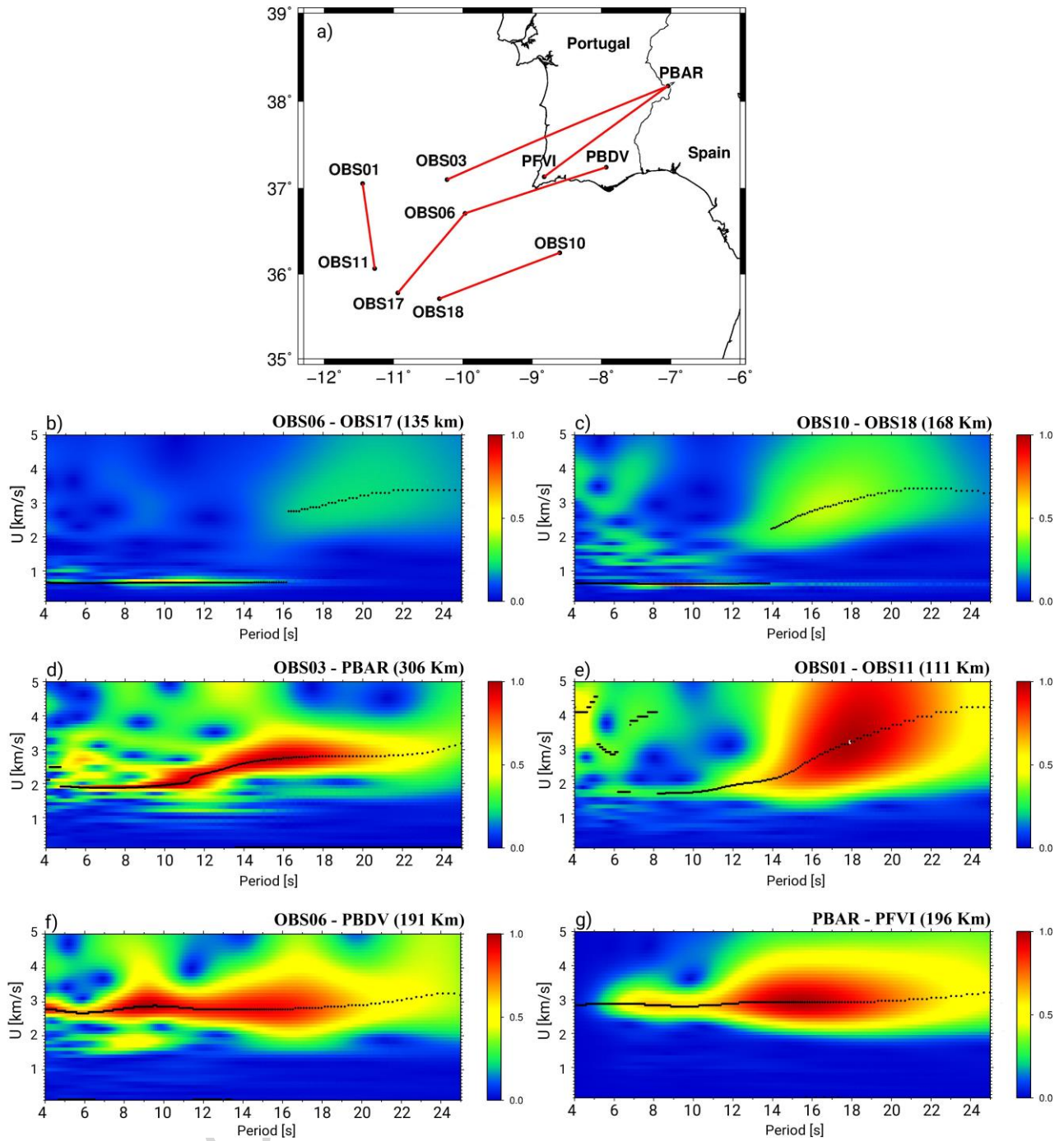
**Fig. 2.** Normalized power spectra of OBS03 and land station MESJ during the NEAREST campaign. The secondary and primary microseismics bands clearly show the contribution of oceanic storms, however, on the OBS vertical seismometer the noise level above 10s is due to tilt noise. The horizontal scale shows the number of days from the start of recording. The relation to calendar days is given below.



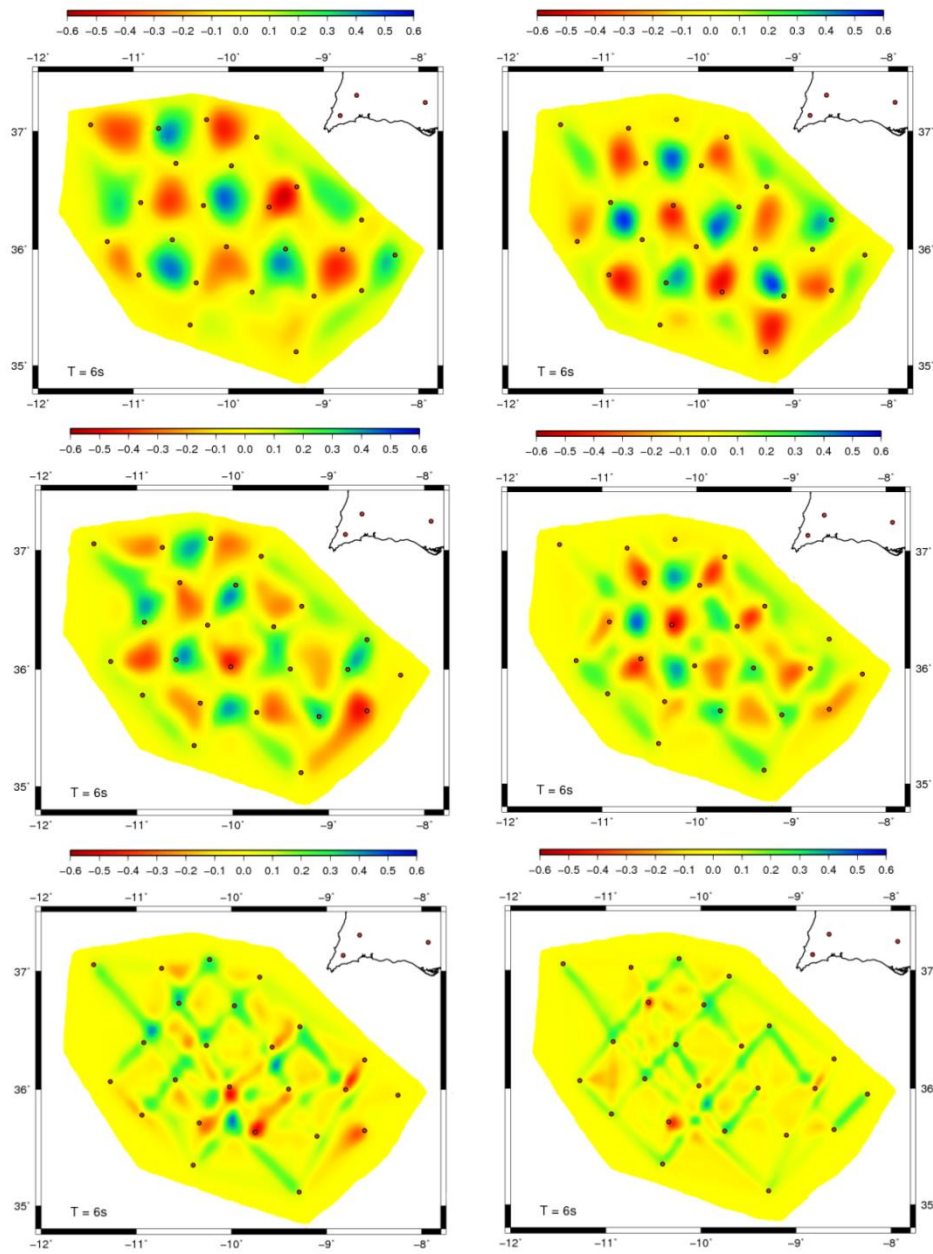
**Fig. 3.** Cross-correlograms for the pair OBS04 (Z) and OBS05 (Z), stacked per month using a combination of 2 sorts of algorithms on both time-domain normalization and stack of the daily cross-correlations. a) 1-bit time domain normalization followed by linear stack; b) 1-bit time domain normalization followed by tf-PWS; c) RAM time domain normalization followed by linear stack; and d) RAM time domain normalization followed by tf-PWS.



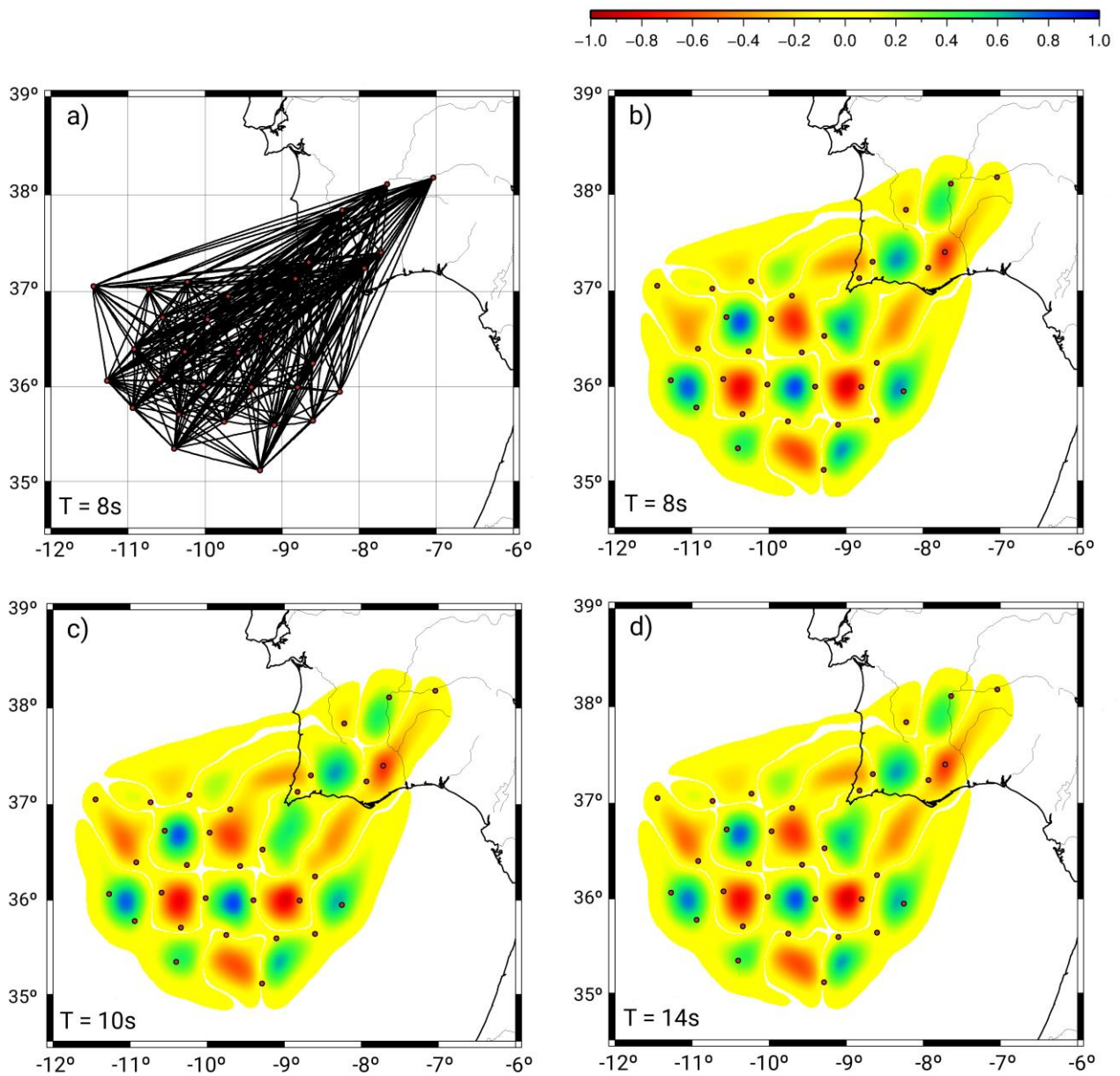
**Fig. 4.** Comparison cross-correlograms stacked per month for all possible channel combinations between OBS04 and OBS05: a) OBS04(Z) - OBS05(Z); b) OBS04(H) - OBS05(Z); c) OBS04(Z) - OBS05(H); d) OBS04(H) - OBS05(H).



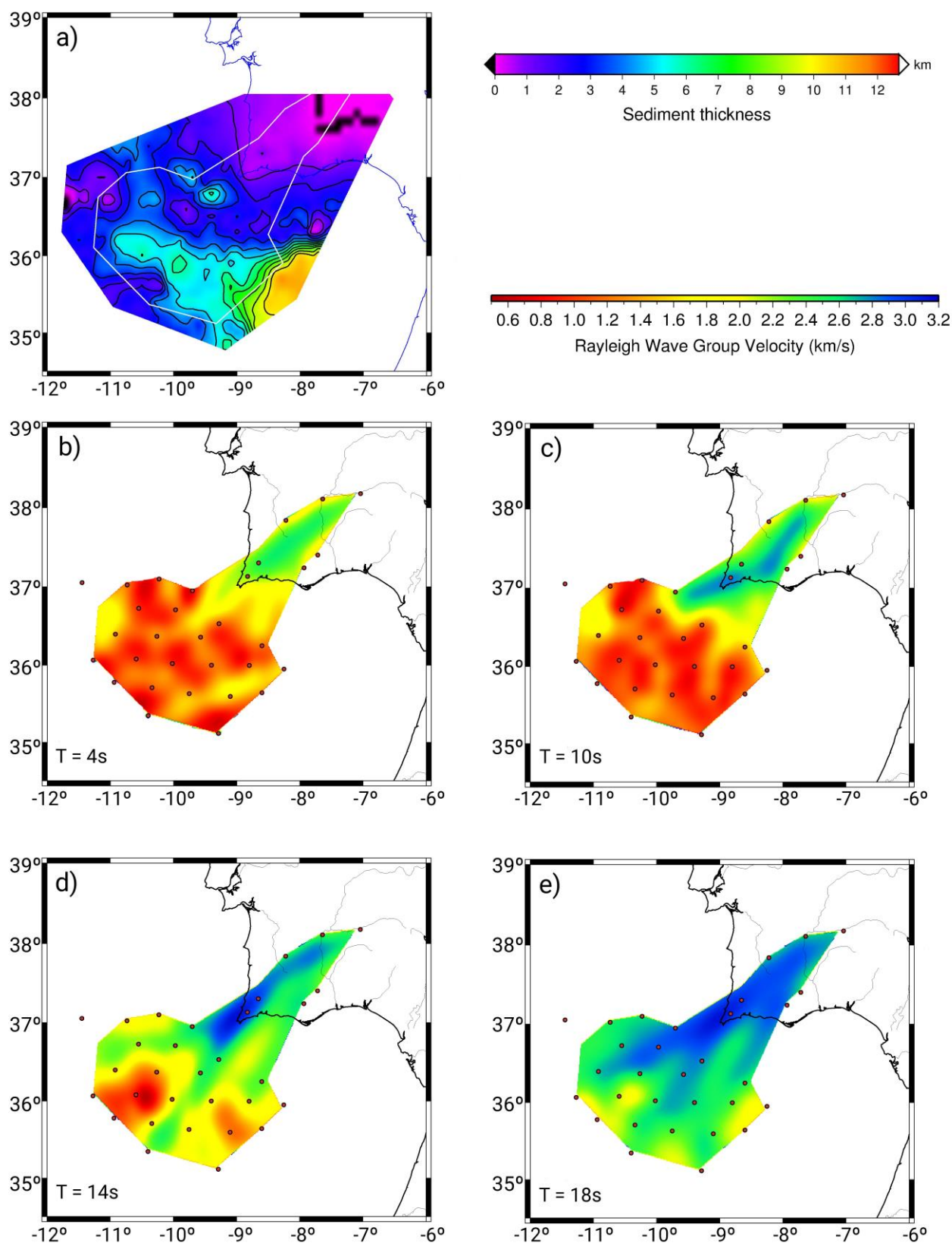
**Fig. 5.** Dispersion measurements of obtained between OBSs and land stations. The referred sites can be identified in Fig. 1a and in the sketch of the presented tracks in the top (a). b) path starting on the Marquês de Pombal Plateau (OBS06) and ending at the Horseshoe Abyssal Plain (OBS17); c) path between the Portimão Plateau (OBS10) and the Horseshoe Valley (OBS18); d) path from D. Henrique Basin (OBS03) to Barrancos, near the Spanish border (PBAR); e) path starting at the Tagus Abyssal Plain (OBS01) towards the Horseshoe Abyssal Plain (OBS11); f) path from the Marquês de Pombal Plateau (OBS06) to Faro, Algarve (PBDV); g) onshore path between Barrancos (PBAR) and Faro (PFVI).



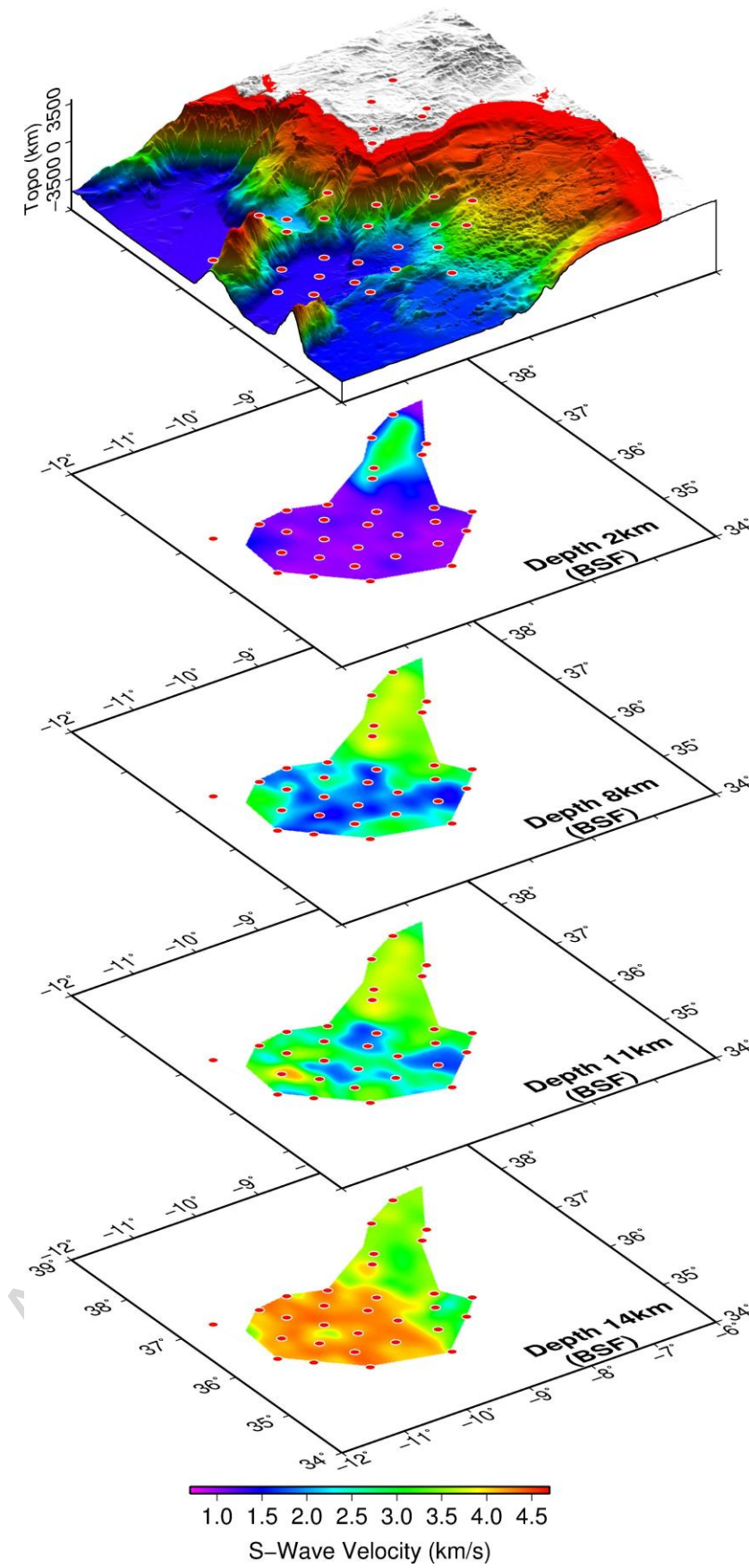
**Fig.6.** Checkboard tests made with different grid size obtained with real data at 6s.



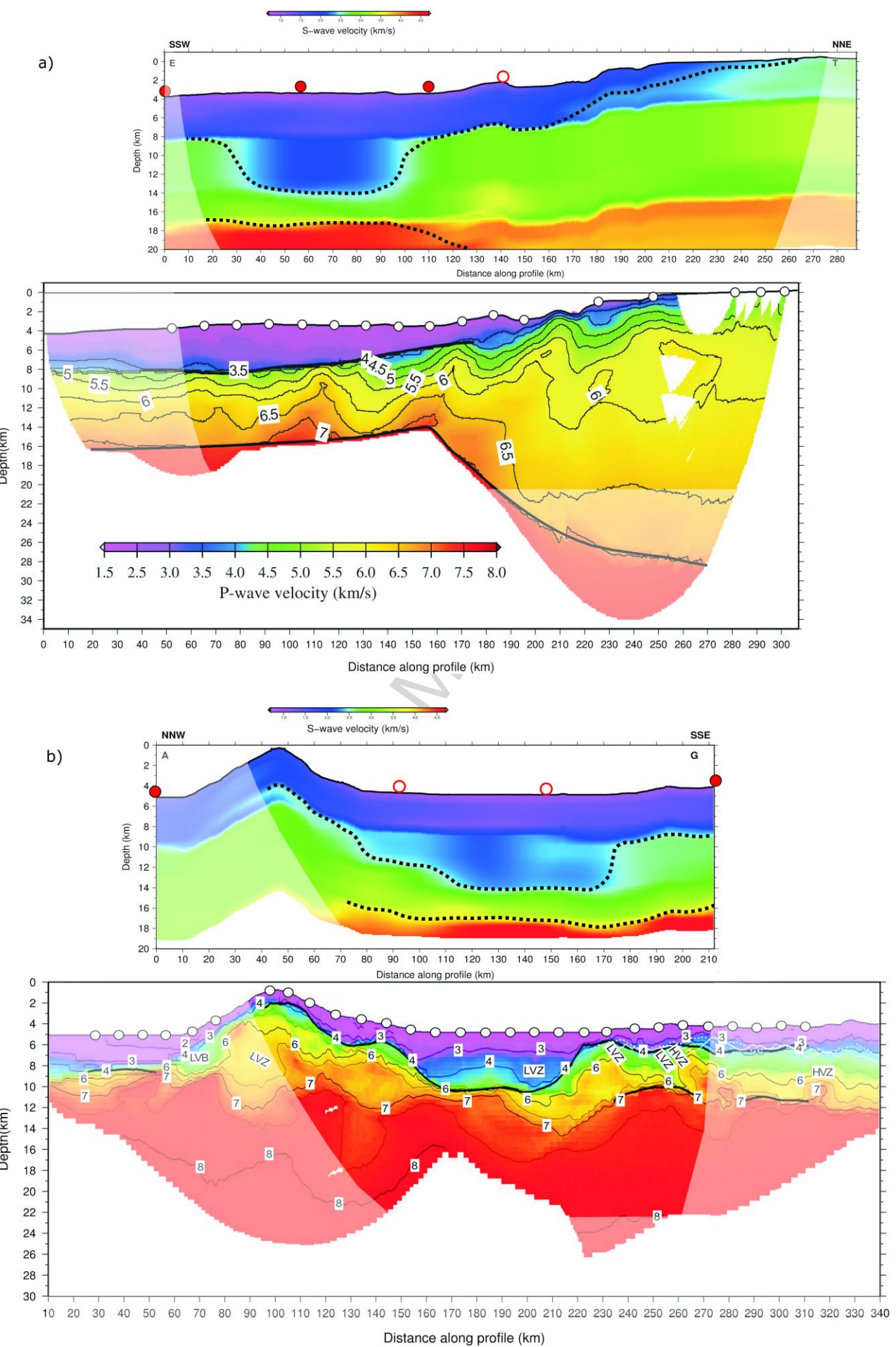
**Fig. 7.** Ray-path coverage used in the inversion for 8 s (a) and checkerboard tests, (b to d) for 8.0, 10.0 and 14.0 s. Seismic stations are represented with red dots. The input model has a grid of  $18.5 \times 18.5 \text{ km}^2$  anomalies and a maximum perturbation of velocity nodes of 1.0 km/s.



**Fig. 8.** a) Sediment thickness from Thiebot and Gutscher (2006). b) to e) or: 4, 10, 14 and 18 s. The values used in the starting homogeneous velocity models were, respectively: 0.7, 0.9, 1.5 and 2.2 km/s. Seismic stations are represented with red dots.

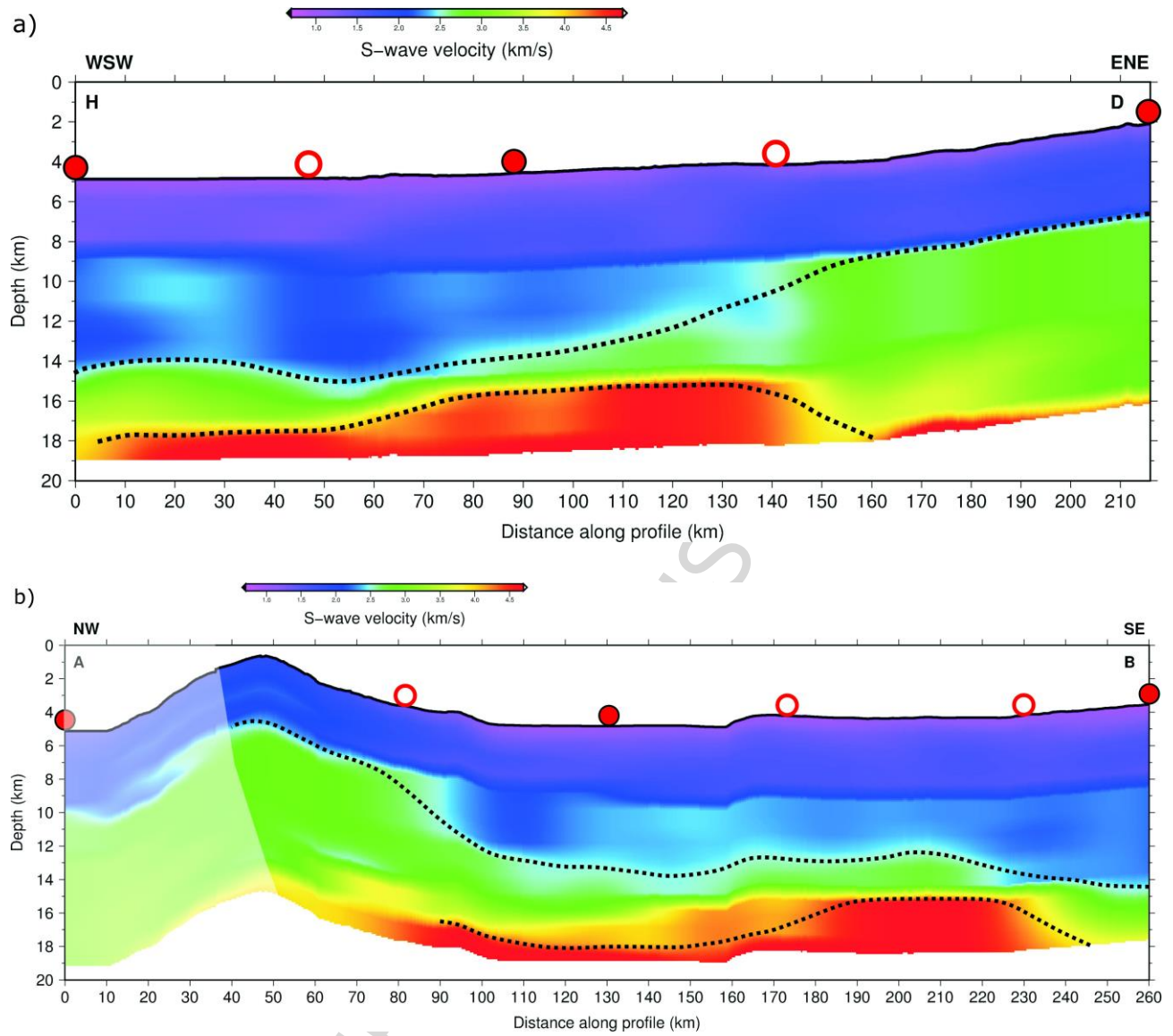


**Fig. 9.** Top: Topographic map of the studied area. Below: Shear wave velocity maps at depths of 2, 8, 11 and 14 km Below Sea Floor (BSF). Seismic stations are represented with red dots.



**Fig. 10.** Comparison of S-wave cross-sections and 2-D velocity models obtained by tomographic inversion of active seismic data. Location of profiles is given in Fig. 1b. a) Cross-section E-T and P-wave model of profile P2 by Sallarès et al. (2011). b) Cross-section AG and P-wave velocity model of profile P1 by Martinez-Loriente (2014). The S-wave colour code is identical to the P-wave code with P velocities divided by 1.7. Circles in the cross-section mark the location of OBS in the passive NEAREST experiment. Open circles are projected locations. The black dashed lines in the cross-section are the interpreted base of sediments and crust-mantle transition.

ACCEPTED MANUSCRIPT



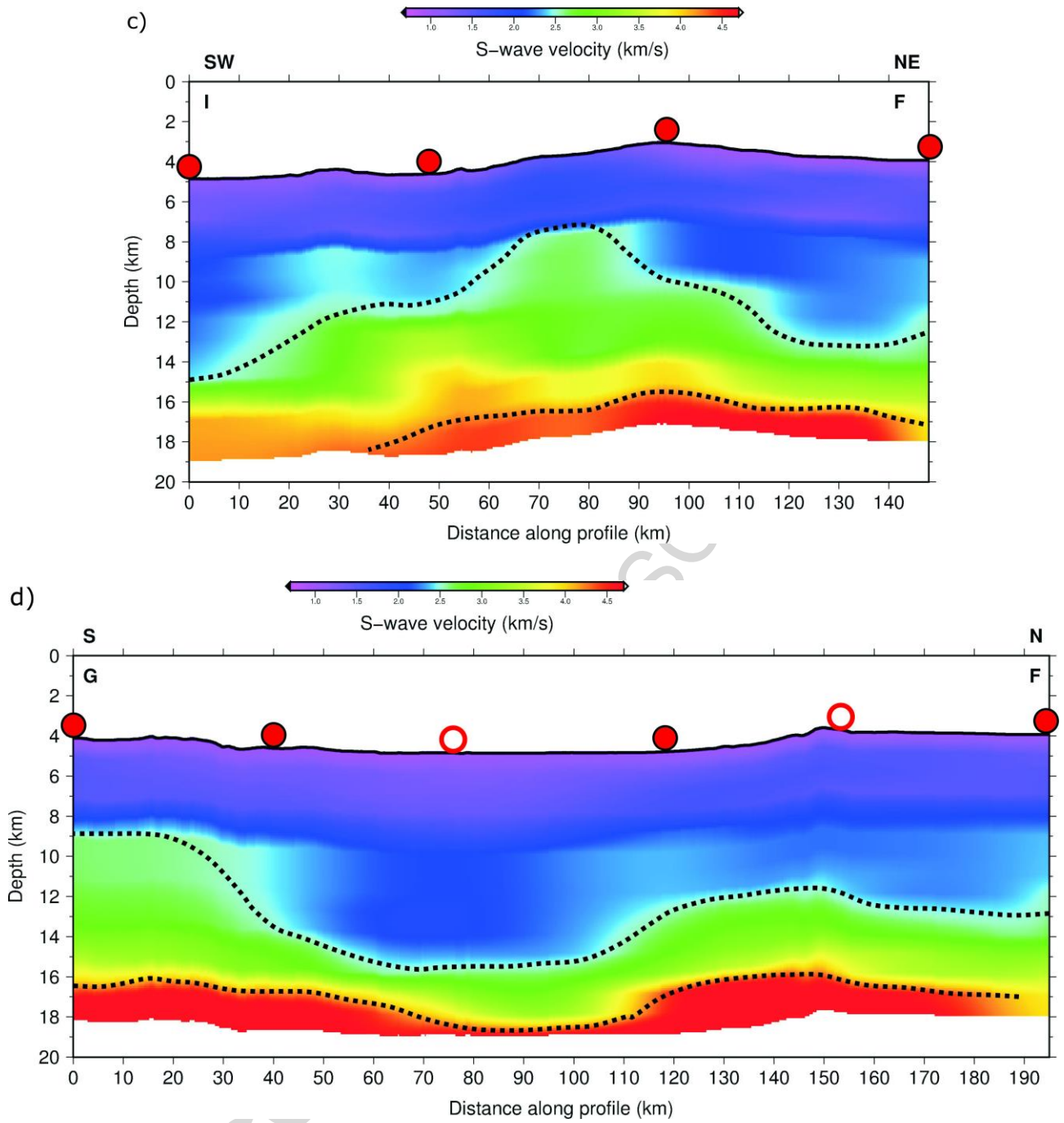


**Fig. 11.** S-wave cross-sections extracted from the tomographic model. The location of profiles is given in Fig. 1b. Red circles mark the location of OBS in the passive NEAREST experiment. Open circles are projected locations. The black dashed lines are the interpreted base of sediments and crust-mantle transition. The S-wave colour code is identical to the P-wave code of Sallarès et al. (2011) with P velocities divided by 1.7. a) Cross-section H-D; b) Cross-section A-B; c) Cross-section I-F; d) Cross-section G-F.